Geophys. J. Int. (2009) **176,** 865–888 doi: 10.1111/j.1365-246X.2008.04010.x

Multimode surface wave sensitivity kernels in radially anisotropic earth media

Ying Zhou

Department of Geosciences, Virginia Tech, Blacksburg, VA 24061, *USA. E-mail: yingz@vt.edu*

Accepted 2008 October 10. Received 2008 October 7; in original form 2008 July 19

SUMMARY

I calculate three-dimensional (3-D) sensitivity kernels of multimode surface wave observables in radially anisotropic earth media for perturbations in wave speeds α_{H}, α_{V}, β_{H}, β_{V} and η as well as in density ρ. The 3-D phase-delay and amplitude kernels are formulated based upon Born approximation in the framework of surface wave mode summation, fully accounting for cross-branch mode coupling. Long-period, multimode, surface wave sensitivity kernels show structures of multiple reflected body waves. Jean's relation can be applied to quantify the 'mode-ray duality' of multimode surface waves and provide guidelines for measurement-window determination.

Key words: Surface waves and free oscillations; Seismic anisotropy; Seismic tomography; Theoretical seismology; Wave scattering and diffraction.

1 INTRODUCTION

In the past several decades, ray-theoretical tomographic studies have made great contributions in advancing our understanding of the Earth's deep interior. Seismic ray theory is based upon a high-frequency approximation, it breaks down when the length scale of lateral heterogeneities is small compared to the characteristic wavelength of the seismic waves. To overcome this resolution limits, efforts have been made to develop finite-frequency theory to account for diffractional effects in wave propagation based upon first-order Born approximation (e.g. Woodhouse & Girnius 1982; Snieder & Nolet 1987; Romanowicz 1987; Yomogida & Aki 1987; Meier *et al.* 1997; Marquering *et al.* 1998; Dahlen *et al.* 2000; Dalkolmo & Friederich 2000; Hung *et al.* 2000; Zhao *et al.* 2000; Spetzler *et al.* 2002; Zhou *et al.* 2004; Tromp *et al.* 2005; Yoshizawa & Kennett 2005; Liu & Tromp 2008). High-resolution global models based upon 3-D Born sensitivity kernels have been recently derived from delay-time measurements of body waves as well as fundamental-mode surface waves (e.g. Montelli *et al.* 2004; Zhou *et al.* 2006).

Higher-mode surface waves (overtones) play an important role in imaging the Earth's interior in that they provide complementary depth coverage to deep-turning body waves and fundamental-mode surface waves, especially in the mid-mantle roughly between ∼250 and ∼1500 km. Surface wave overtones have been widely used in global and regional tomographic studies based upon seismic ray theory (e.g. Stutzmann & Montagner 1994; van Heijst & Woodhouse 1999; Simons *et al.* 2002; Lebedev & Nolet 2003). A variety of approaches have been proposed to utilize the dispersive nature of higher-mode surface waves. The main difficulty associated with overtone measurements is that different overtone modes can arrive simultaneously in the seismogram within a narrow frequency band, making it difficult to extract a single overtone mode (e.g. Lerner-Lam & Jordan 1983; Nolet 1990; Li & Romanowicz 1996; van Heijst & Woodhouse 1997). In this paper, I develop first-order Born theory for multimode surface wave observables, that is, phase-delay and amplitude measurements made between data and (fully mode-summed) synthetics without isolating any single overtone modes. The theory also applies to single-mode measurement as a special case; and, in the case of single-mode measurement, I show that 3-D volumetric sensitivity kernels can be reduced to 2-D phase velocity kernels.

Radial anisotropy (or transversely isotropy) is hexagonally symmetric anisotropy with the axis of symmetry being radial (vertical). Radial anisotropy in the upper mantle has been widely observed in surface wave studies since the early 1960s (e.g. Anderson 1961; Aki & Kaminuma 1963). Dziewonski & Anderson (1981) reported the global average of radial anisotropy in the top 220 km in the Preliminary Reference Earth Model (PREM). Later studies suggest global existence of seismic anisotropy in the lower upper mantle, the transition zone as well as in the shallower part of the lower mantle (e.g. Montagner & Kennett 1996; Beghein & Trampert 2003; Panning & Romanowicz 2006; Zhou *et al.* 2006). Based upon adjoint methods, Sieminski *et al.* (2007) investigated finite-frequency sensitivity of fundamental-mode surface wave cross-correlation measurements to perturbations in anisotropic parameters. In the presence of radial anisotropy, seismic waves of different polarizations can be strongly coupled and the coupling is more significant for higher-mode surface waves than for fundamental-mode surface waves. In the calculation of multimode sensitivity kernels, I fully account for mode coupling in radially anisotropic earth media.

I develop 3-D Born sensitivity kernels for multimode, surface wave phase-delay and amplitude measurements made on windowed seismograms (with interested wavepacks in the measurement window). In practice, tapering techniques can be applied to make

measurements more stable and reliable. Following Zhou *et al.* (2004), I formulate 3-D Born sensitivity kernels for multitaper measurements, which also apply to measurements made with single tapers (e.g. a boxcar taper) as a special case. The derivation of Born sensitivity kernels in this paper can be viewed as a generalization of the theory of Zhou *et al.* (2004) to allow for perturbations in radial anisotropy. Much of the discussions in this paper is focused on phase delays made on windowed seismograms where overtone energy dominates within the measurement window. I show that Born sensitivity kernels of long-period, multimode measurements exhibit 3-D structures of multiple-reflected body waves as a result of coupling among overtone modes. The 'mode-ray duality' of multimode surface waves will be discussed in Section 9. The 3-D multimode kernels can be computed very efficiently using a fast computation scheme that will be documented in a second paper (Zhou, in preparation). All examples of multimode kernels shown in this paper are calculated with full mode coupling.

2 EQUATIONS OF MOTION, GREEN'S TENSOR AND MOMENT TENSOR RESPONSE

In this section, I review basic equations of surface wave mode theory to establish a notation for the consideration of multimode Born approximation in anisotropic media in Section 3. Whenever possible, I try to follow the same notation as used in an early paper on surface wave Born theory in isotropic media by Zhou *et al.* (2004).

Consider an elastic earth model occupying a volume $\oplus$ with surface $\partial\oplus$. The model may have a number of internal solid-solid discontinuities and fluid–solid discontinuities, denoted by $\Sigma_{\rm SS}$ and $\Sigma_{\rm FS}$, respectively. The union of all the boundary, including the outer free surface $\partial\oplus$, will be denoted by $\Sigma = \partial\oplus + \Sigma_{\rm SS} + \Sigma_{\rm FS}$. Let $\mathbf{G}_{\rm rs}(\omega)$ be the Green's tensor, or displacement response at the receiver $\mathbf{x}_{\rm r} = (r_{\rm r}, \theta_{\rm r}, \phi_{\rm r})$ to an impulsive source at the source $\mathbf{x}_{\rm s} = (r_{\rm s}, \theta_{\rm s}, \phi_{\rm s})$. The Green's tensor satisfies the elastodynamic equation

$$-\omega^2\rho\mathbf{G}_{\rm rs} - \nabla\cdot[\mathbf{C}:\nabla\mathbf{G}_{\rm rs}] = \mathbf{I}\,\delta(\mathbf{x}-\mathbf{x}_{\rm s}) \quad \text{in } \oplus, \tag{1}$$

as well as dynamic and kinematic boundary conditions:

$$[\hat{\mathbf{n}}\cdot(\mathbf{C}:\nabla\mathbf{G}_{\rm rs})]^+_- = 0 \quad \text{on } \Sigma, \quad [\mathbf{G}_{\rm rs}]^+_- = 0 \quad \text{on } \Sigma_{\rm SS}, \quad \text{and}$$
$$[\mathbf{n}\cdot\mathbf{G}_{\rm rs}]^+_- = 0 \quad \text{on } \Sigma_{\rm FS}, \tag{2}$$

where $\hat{\mathbf{n}}$ is the unit vector normal to the boundary, the quantity $\mathbf{C}$ is the fourth-order elastic tensor, and $\mathbf{I}$ is the identity matrix. The quantities ω and ρ are the angular frequency of the seismic wave and the density of the elastic media, respectively. The far-field surface wave Green's tensor $\mathbf{G}_{\rm rs}(\omega)$ can be written as a summation over all surface wave modes σ (Snieder & Nolet 1987; Dahlen & Tromp 1998, section 11.3):

$$\mathbf{G}_{\rm rs}(\omega) = \sum_\sigma \frac{\mathbf{p}_{\rm r}\mathbf{p}_{\rm s}^*\, e^{-i\,(k\Delta - n\pi/2+\pi/4)}}{\sqrt{8\pi k|\sin\Delta|}}, \tag{3}$$

where Δ is source–receiver angular arclength, and the integer n is the polar passage index (e.g. $n=0$ for minor arc and $n=1$ for major arc). The quantity k is angular wavenumber of mode σ. The vector $\mathbf{p} = \hat{\mathbf{r}}U - i\hat{\mathbf{k}}V + i(\hat{\mathbf{r}}\times\hat{\mathbf{k}})W$ is surface wave polarization vector of mode σ with $U(r)$, $V(r)$ and $W(r)$ being the vertical, radial and transverse displacement eigenfunctions (Snieder & Nolet 1987). The roman subscribe r and s denotes quantities evaluated at the receiver $\mathbf{x}_{\rm r}$ and the source $\mathbf{x}_{\rm s}$, respectively. The asterisk denotes the complex conjugate. We have applied the same normalization in eq. (3) as in Tromp & Dahlen (1992) and Zhou *et al.* (2004).

For a moment tensor seismic source, displacement at the receiver can be written as (Dahlen & Tromp 1998)

$$s(\omega) = (i\omega)^{-1}\left[\,\mathbf{M}:\nabla_{\rm s}\mathbf{G}^{\rm T}_{\rm rs}(\omega)\,\right]\cdot\hat{\mathbf{v}}, \tag{4}$$

where $\mathbf{M}$ is the second-order moment tensor, the quantity $\hat{\mathbf{v}}$ is the unit vector describing the polarization of the seismometer at the receiver, and the superscript T denotes the transpose over the first and second indices of a tensor. To lowest order, the gradient $\nabla_{\rm s}$ operator acts only upon the oscillatory term $e^{-ik\Delta}$ in eq. (3) and upon the polarization vector at the source $\mathbf{p}_{\rm s}$, yielding (Zhou *et al.* 2004),

$$s(\omega) = \sum_\sigma \underbrace{\mathcal{S}}_{\substack{\text{source}\\ \text{radiation}}} \times \underbrace{\left(\frac{e^{-i(k\Delta - n\pi/2+\pi/4)}}{\sqrt{8\pi k|\sin\Delta|}}\right)}_{\text{geometrical ray path}} \times \underbrace{\mathcal{R}}_{\substack{\text{receiver}\\ \text{polarization}}}. \tag{5}$$

The source radiation term $\mathcal{S} = (i\omega)^{-1}(\mathbf{M}:\mathbf{E}^*_{\rm s})$, where the quantity $\mathbf{E}$ is the so-called 'surface wave strain tensor' (Dahlen & Tromp 1998, section 11.4), and the quantity $\mathcal{R} = \mathbf{p}_{\rm r}\cdot\hat{\mathbf{v}}$ is the receiver term. Detailed expressions of both the source radiation term $\mathcal{S}$ and the receiver term $\mathcal{R}$ can can be found in Appendix A.

3 BORN APPROXIMATION IN RADIALLY ANISOTROPIC MEDIA

In radially anisotropic media, the forth-order elastic tensor $\mathbf{C}$ can be described by five independent elastic parameters: A, C, N, L and F (Love 1927). The relation between the elastic parameters and wave speeds can be written as

$$\alpha_{\rm H} = \sqrt{A/\rho}, \quad \alpha_{\rm V} = \sqrt{C/\rho}, \quad \beta_{\rm H} = \sqrt{N/\rho},$$
$$\beta_{\rm V} = \sqrt{L/\rho}, \quad \eta = F/(A-2L), \tag{6}$$

where $\alpha_{\rm H}$ and $\alpha_{\rm V}$ are the wave speeds of horizontally polarized and vertically polarized P waves, respectively; and $\beta_{\rm H}$ and $\beta_{\rm V}$ are the wave speeds of horizontally polarized and vertically polarized shear waves, respectively; The fifth parameter η describes the speed of waves propagating in an intermediate direction.

Consider a spherically symmetric reference earth model where density and elastic parameters depend only upon the radius r. This reference model is then subjected to an infinitesimal perturbation in density and elastic tensor

$$\rho \to \rho + \delta\rho, \quad \mathbf{C} \to \mathbf{C} + \delta\mathbf{C}, \tag{7}$$

where the latter can be described by perturbations in the five elastic parameters:

$$A \to A + \delta A, \quad C \to C + \delta C, \quad N \to N + \delta N,$$
$$L \to L + \delta L, \quad F \to F + \delta F, \tag{8}$$

and the associated perturbations in wave speeds are

$$\alpha_{\rm H} \to \alpha_{\rm H} + \delta\alpha_{\rm H}, \quad \alpha_{\rm V} \to \alpha_{\rm V} + \delta\alpha_{\rm V}, \quad \beta_{\rm H} \to \beta_{\rm H} + \delta\beta_{\rm H},$$
$$\beta_{\rm V} \to \beta_{\rm V} + \delta\beta_{\rm V}, \quad \eta \to \eta + \delta\eta. \tag{9}$$

3.1 Born approximation—perturbed Green's tensor

In response to perturbations in density and elastic constants, the associated surface wave Green's tensor is perturbed by

$$\mathbf{G}_{\rm rs}(\omega) \to \mathbf{G}_{\rm rs}(\omega) + \delta\mathbf{G}_{\rm rs}(\omega). \tag{10}$$

Based upon first-order Born approximation (correct to first order perturbations in $\delta\rho$ and $\delta\mathbf{C}$), the Green's tensor perturbation $\delta\mathbf{G}_{\rm rs}(\omega)$ can be found by solving a perturbed version of eq. (1):

$$-\omega^2\rho\,\delta\mathbf{G}_{\rm rs} - \nabla\cdot(\mathbf{C}:\nabla\delta\mathbf{G}_{\rm rs}) = \delta\rho\,\omega^2\,\mathbf{G}_{\rm rs} + \nabla\cdot(\delta\mathbf{C}:\nabla\mathbf{G}_{\rm rs}) \quad \text{in } \oplus, \tag{11}$$

subject to the following boundary conditions:

$$\begin{aligned}[\hat{\mathbf{n}}\cdot(\mathbf{C}:\nabla\delta\mathbf{G}_{\rm rs})]^+_- &= -[\hat{\mathbf{n}}\cdot(\delta\mathbf{C}:\nabla\mathbf{G}_{\rm rs})]^+_- \quad \text{on } \Sigma\\ [\delta\mathbf{G}_{\rm rs}]^+_- &= 0 \quad \text{on } \Sigma_{\rm SS},\\ [\mathbf{n}\cdot\delta\mathbf{G}_{\rm rs}]^+_- &= 0 \quad \text{on } \Sigma_{\rm FS}.\end{aligned} \tag{12}$$

Upon using representation theorem (Aki & Richards 2002), the Green's tensor perturbation $\delta\mathbf{G}_{\rm rs}(\omega)$ can be written as a combination of volumetric and surface integrations

$$\delta\mathbf{G}_{\rm rs} = \iiint_{\oplus}\mathbf{G}_{\rm rx}\cdot\left[\delta\rho\,\omega^2\,\mathbf{G}_{\rm xs} + \nabla\cdot(\delta\mathbf{C}:\nabla\mathbf{G}_{\mathbf{xs}})\right]\mathrm{d}^3\mathbf{x} - \iint_{\Sigma}\mathbf{G}_{\rm rx}\cdot[\hat{\mathbf{n}}\cdot(\delta\mathbf{C}:\nabla\mathbf{G}_{\mathbf{xs}})]^+_-\,\mathrm{d}\Sigma. \tag{13}$$

Gaussian theorem (first Green's identify) can be applied to eliminate the surface integrations in eq. (13), yielding,

$$\delta\mathbf{G}_{\rm rs} = \iiint_{\oplus}\left[\delta\rho\,\omega^2\,\mathbf{G}_{\rm rx}\cdot\mathbf{G}_{\rm xs} - \nabla_{\rm x}\mathbf{G}_{\rm rx}:\delta\mathbf{C}:\nabla\mathbf{G}_{\rm xs}\right]\mathrm{d}^3\mathbf{x} \tag{14}$$

where $\nabla_{\boldsymbol{x}}$ is the spatial gradient with respect to $\mathbf{x}$.

Upon substituting the normalized surface wave Green's tensor (eq. 3), the perturbed Green's tensor can be written as a double summation over all surface wave modes σ' and σ'' as

$$\delta\mathbf{G}_{\rm rs}(\omega) = \sum_{\sigma'}\sum_{\sigma''}\iiint_{\oplus}\frac{\mathbf{p}'^{*}_{\rm s}\,\mathbf{p}''_{\rm r}\;e^{-i\,[k'\Delta'+k''\Delta''-(n'+n''-1)\pi/2]}}{\sqrt{8\pi k'|\sin\Delta'|}\;\sqrt{8\pi k''|\sin\Delta''|}}\,{}_{\sigma'}\Omega_{\sigma''}\;\mathrm{d}^3\mathbf{x}, \tag{15}$$

where the single prime$'$ indicates the source-to-scatterer leg of the scattered wave, and the double prime$''$ indicates the scatterer-to-receiver leg of the scattered wave (Fig. A1). The interaction term ${}_{\sigma'}\Omega_{\sigma''}(\mathbf{x},\omega)$ represents the strength of scattering at the scatterer $\mathbf{x}$,

$${}_{\sigma'}\Omega_{\sigma''} = \delta\rho\,\omega^2\,(\mathbf{p}'\cdot\mathbf{p}''^{*}) - \mathbf{E}''^{*}:\delta\mathbf{C}:\mathbf{E}', \tag{16}$$

where $\mathbf{E}'$ is the 'surface wave strain tensor' of surface wave mode σ' in the source-to-scatterer leg, and E$''$ is the 'surface wave strain tensor' of surface wave mode σ'' in the scatterer-to-receiver leg, both evaluated at the scatterer $\mathbf{x}$. The interaction term ${}_{\sigma'}\Omega_{\sigma''}(\mathbf{x},\omega)$ has linear dependence upon fractional model perturbations

$${}_{\sigma'}\Omega_{\sigma''} = {}_{\sigma'}\Omega^{m}_{\sigma''}\delta m = {}_{\sigma'}\Omega^{\alpha_{\rm H}}_{\sigma''}\left(\frac{\delta\alpha_{\rm H}}{\alpha_{\rm H}}\right) + {}_{\sigma'}\Omega^{\alpha_{\rm V}}_{\sigma''}\left(\frac{\delta\alpha_{\rm V}}{\alpha_{\rm V}}\right) + {}_{\sigma'}\Omega^{\beta_{\rm H}}_{\sigma''}\left(\frac{\delta\beta_{\rm H}}{\beta_{\rm H}}\right) + {}_{\sigma'}\Omega^{\beta_{\rm V}}_{\sigma''}\left(\frac{\delta\beta_{\rm V}}{\beta_{\rm V}}\right) + {}_{\sigma'}\Omega^{\eta}_{\sigma''}\left(\frac{\delta\eta}{\eta}\right) + {}_{\sigma'}\Omega^{\rho}_{\sigma''}\left(\frac{\delta\rho}{\rho}\right), \tag{17}$$

where we have used a shorthand notation for model perturbations

$$\delta m: \quad \text{shorthand for} \quad \delta\alpha_{\rm H}/\alpha_{\rm H},\ \delta\alpha_{\rm V}/\alpha_{\rm V},\ \delta\beta_{\rm H}/\beta_{\rm H},\ \delta\beta_{\rm V}/\beta_{\rm V},\ \delta\eta/\eta,\ \delta\rho/\rho. \tag{18}$$

The quantities ${}_{\sigma'}\Omega^{\alpha_{\rm H}}_{\sigma''}(\mathbf{x},\omega)$, ${}_{\sigma'}\Omega^{\alpha_{\rm V}}_{\sigma''}(\mathbf{x},\omega)$, ${}_{\sigma'}\Omega^{\beta_{\rm H}}_{\sigma''}(\mathbf{x},\omega)$, ${}_{\sigma'}\Omega^{\beta_{\rm V}}_{\sigma''}(\mathbf{x},\omega)$, ${}_{\sigma'}\Omega^{\eta}_{\sigma''}(\mathbf{x},\omega)$ and ${}_{\sigma'}\Omega^{\rho}_{\sigma''}(\mathbf{x},\omega)$ are the 'scattering coefficients'—they represent the 'strength' of scattering due to perturbations in wave speeds $\alpha_{\rm H}$, $\alpha_{\rm V}$, $\beta_{\rm H}$, $\beta_{\rm V}$, η and density ρ at the scatterer x. The dependence of the scattering coefficients ${}_{\sigma'}\Omega^{m}_{\sigma''}$ upon the scattering angle ψ (Fig. A1) is given in Appendix B.

3.2 Perturbed moment tensor seismogram and waveform kernels

In response to perturbations in wave speeds and density, the displacement at the receiver is perturbed by

$$s(\omega)\to s(\omega)+\delta s(\omega), \tag{19}$$

where $s(\omega)$ is the displacement in the unperturbed earth model, and $\delta s(\omega)$ is the displacement of scattered wave due to model perturbations. The scattered wave $\delta s(\omega)$ generated by a moment tensor source $\mathbf{M}(\omega)$ can be obtained from the Green's tensor perturbation $\delta\mathbf{G}_{\rm rs}(\omega)$ via the analogue of eq. (4):

$$\delta s(\omega) = (i\omega)^{-1}\,\mathbf{M}:\nabla_{\rm s}\left[\delta\mathbf{G}^{\rm T}_{\rm rs}(\omega)\right]\cdot\hat{\boldsymbol{\nu}}. \tag{20}$$

Upon substituting the expression of $\delta\mathbf{G}_{\rm rs}(\omega)$ (eq. 15) and making the same approximation to the spatial gradient operator $\nabla_{\rm s}$ as in eq. (5), the displacement seismogram of the scattered wave $\delta s(\omega)$ can be written as a 3-D integration over all model perturbations in the earth:

$$\delta s(\omega) = \iiint_{\oplus}\mathcal{K}^{m}(\mathbf{x},\omega)\;\delta m(\mathbf{x})\,\mathrm{d}^3\mathbf{x}, \tag{21}$$

where $\mathcal{K}^{m}(\mathbf{x},\omega)$ is the complex integration kernel of the displacement of the scattered wave,

$$\mathcal{K}^{m}(\mathbf{x},\omega) = \sum_{\sigma'}\sum_{\sigma''}\mathcal{S}'\left[\frac{e^{-i\,(k'\Delta'-n'\pi/2+\pi/4)}}{\sqrt{8\pi k'|\sin\Delta'|}}\right]{}_{\sigma'}\Omega^{m}_{\sigma''} \times\left[\frac{e^{-i\,(k''\Delta''-n''\pi/2+\pi/4)}}{\sqrt{8\pi k''|\sin\Delta''|}}\right]\mathcal{R}''. \tag{22}$$

The quantity $\mathcal{S}'$ is the source term of the scattered wave, that is, source excitation of the surface wave mode σ' that travels from the source to the scatterer, and $\mathcal{R}''$ is the receiver term of the scattered wave, and is dependent upon the arrival angle of the surface wave mode σ'' that travels from the scatterer to the receiver. Detailed expressions of the source term $\mathcal{S}'$ and receiver term $\mathcal{R}''$ of the scattered wave can be found in Appendix A.

4 MULTITAPER MEASUREMENTS AND SENSITIVITY KERNELS

The complex moment tensor displacement seismogram in the reference earth model can be written as

$$s(\omega) = \mathcal{A}(\omega)e^{-i\phi(\omega)} \quad \text{in reference earth model}, \tag{23}$$

where $\mathcal{A}(\omega)$ and $\phi(\omega)$ are the amplitude and phase of the reference seismogram, respectively. The perturbed seismogram can be expressed in terms of perturbations in the amplitude and the phase,

$$s(\omega)\to s(\omega)+\delta s(\omega) = [\mathcal{A}(\omega)+\delta\mathcal{A}(\omega)]\,e^{-i\,[\phi(\omega)+\delta\phi(\omega)]} \quad \text{in perturbed earth model}, \tag{24}$$

where $\delta\phi(\omega)$ and $\delta\mathcal{A}(\omega)$ are the frequency-dependent phase delay and amplitude perturbation of the perturbed (observed) displacement seismogram with respect to the reference seismogram. Frequency-dependent phase-delay (dispersion) measurements $\delta\phi(\omega)$ have been widely used in surface wave tomography; in additional to phase delays, frequency-dependent amplitude perturbations $\delta\mathcal{A}(\omega)$ can been used as secondary observables to provide complementary constraints on the Earth's 3-D elastic structure (e.g. Laske & Masters 1996). While both phase-delay and amplitude measurements can be made by comparing the spectra between

the reference seismogram and the data, spectral estimates made on windowed seismogram with finite timelength is subjected to spectral leakage. Therefore, in formulating sensitivity kernels for phase-delay and amplitude measurements, considerations need to be taken to account for spectra averaging introduced by seismogram windowing and/or additional tapering techniques applied in making measurements.

In this paper, I follow the analysis of Zhou *et al.* (2004), and formulate sensitivity kernels of phase-delay and amplitude measurements made with a multitaper technique—which also apply to any single-taper (e.g. a boxcar taper) measurements as a special case. It has been suggested that measurements made with a multi taper technique (Thomson 1982) have better resistance to spectral bias in surface wave studies (Laske & Masters 1996). The main advantages of the multitaper technique are that the tapers are prolate spheroidal eigentapers (Slepian 1978) with narrowly concentrated spectra, and, they are orthogonal to each other. A reliable spectral estimate can be obtained by least-square fitting of independent measurements; furthermore, these independent measurements provide good estimates of measurement errors introduced by spectra leakage.

Following Zhou *et al.* (2004), phase delays and amplitude perturbations determined by least-square fitting of multitaper estimates can be written, correct to first order in the small perturbations, as,

$$\delta\phi(\omega) = -\mathrm{Im}\left(\frac{\sum_j \delta s_j\, s_j^*}{\sum_j s_j\, s_j^*}\right), \quad \delta \ln \mathcal{A}(\omega) = \mathrm{Re}\left(\frac{\sum_j \delta s_j\, s_j^*}{\sum_j s_j\, s_j^*}\right), \tag{25}$$

where $\delta \ln \mathcal{A}(\omega) = \delta\mathcal{A}(\omega)/\mathcal{A}(\omega)$ is the fractional amplitude perturbation, and $\delta\phi(\omega)$ is the phase delay, both measured with a set of multitapers through least-square fitting (Laske & Masters 1996). The quantity $s_j(\omega) = s(\omega) \otimes h_j(\omega)$ is the spectrum of the tapered reference waveform, where $h_j(\omega)$ is the spectra of the jth taper, and $\otimes$ is a convolution operator. The quantity $\delta s_j(\omega) = \delta s(\omega) \otimes h_j(\omega)$ is the tapered spectra of the scattered waveform. The summation j is over all the tapers. Note that seismogram tapering—multiplication of a seismogram in time domain with taper $h_j(t)$—corresponds to convolution in the spectral domain.

Upon substituting expressions of the scattered waveform $\delta s(\omega)$ (eqs 21–22), the multitaper phase-delay and amplitude measurements as defined in eq. (25) can be written as volumetric integrations over model perturbations,

$$\begin{aligned}\delta\phi(\omega) &= \iiint_{\oplus} K_\phi^m(\mathbf{x}, \omega)\, \delta m(\mathbf{x})\, \mathrm{d}\mathbf{x}^3,\\ \delta \ln A(\omega) &= \iiint_{\oplus} K_A^m(\mathbf{x}, \omega)\, \delta m(\mathbf{x})\, \mathrm{d}\mathbf{x}^3,\end{aligned} \tag{26}$$

and the associated phase and amplitude sensitivity kernels are

$$K_\phi^m(\mathbf{x}, \omega) = -\mathrm{Im}\left[\frac{\sum_j \mathcal{K}_j^m(\mathbf{x}, \omega) s_j^*(\omega)}{\sum_j s(\omega) s_j^*(\omega)}\right], \tag{27}$$

$$K_A^m(\mathbf{x}, \omega) = \mathrm{Re}\left[\frac{\sum_j \mathcal{K}_j^m(\mathbf{x}, \omega) s_j^*(\omega)}{\sum_j s(\omega) s_j^*(\omega)}\right], \tag{28}$$

where

$$\mathcal{K}_j^m(\mathbf{x}, \omega) = \mathcal{K}^m(\mathbf{x}, \omega) \otimes h_j(\omega) \tag{29}$$

is tapered complex waveform kernel. The displacement in the unperturbed earth model, $s(\omega)$, and the complex kernel of the scattered waveform, $\mathcal{K}^m(\mathbf{x}, \omega)$, are given in eqs (5) and (22).

In the case of single-taper (e.g. a boxcar taper) measurements, the summation over tapers in eqs (27) and (28) can be dropped. In Section 7, I show that when the taper spectra becomes a Dirac delta function, the above phase and amplitude kernels reduce to single-frequency kernels as given by Zhou *et al.* (2004). It is worth pointing out that single-frequency sensitivity kernels do not have direct practical applications as measurements made on a finite timelength seismogram always involves frequency averaging.

5 SINGLE-MODE KERNELS IN RADIALLY ANISOTROPIC EARTH

In this section, I show examples of single-mode sensitivity kernels to illustrate basic diffractional properties of single-mode surface waves in the presence of anisotropy, as well as to understand variations in single-mode sensitivity as the mode order (N) increases. As mentioned earlier, it is practically difficult to measure the dispersion of a single overtone mode due to simultaneous multimode arrivals. Sensitivity kernels of multimode measurements—measurements made between data and (fully mode-summed) synthetics—will be discussed in Section 6.

The single-mode sensitivity kernels shown in this section are calculated using eqs (27)–(29). In computing single-mode sensitivity kernels, only a single mode is considered in calculating both the reference waveform $s(\omega)$ and the scattered waveform kernel $\mathcal{K}^m(\mathbf{x}, \omega)$, that is, $\sigma_1 = \sigma_2 = \sigma$. Therefore, the summation over modes in the eqs (5) and (22) is dropped. Unless otherwise noted, the reference earth model used in this paper is anisotropic PREM with the surface water layer replaced by underlying upper crust.

Discussions in this section are limited to sensitivity kernels of phase-delay measurements ($\delta\phi$) to perturbations in anisotropic wave speeds α_H, α_V, β_H, β_V and η. Examples of single-mode, surface wave sensitivity to density (ρ) perturbations can be found in Section 6. The sensitivity of amplitude measurements ($\delta \ln \mathcal{A}$) to wave speed perturbations will also be presented in Section 6.

5.1 Love-wave single-mode kernels

In Fig. 1, Love-wave sensitivity kernels $K_\phi^{\beta_\mathrm{H}}$ and $K_\phi^{\beta_\mathrm{V}}$—sensitivity of phase delays to perturbations in wave speeds β_H and β_V—are plotted for fundamental-mode ($N = 0$) as well as for the first three higher-mode ($N = 1, 2, 3$) surface waves. The kernels are computed for measurements made with three $3 - \pi$ Slepian tapers at 10 mHz (100 s). In general, the depth sensitivities as seen in AB depth cross-sections in Fig. 1 agree with 1-D single-mode Frechét kernels (Anderson & Dziewonski 1982): higher-mode surface waves are sensitive to deeper regions than fundamental-mode surface waves; and, the maximum depth of significant sensitivity generally increases with mode order. At 10 mHz, the third higher-mode ($N = 3$) surface wave shows strong sensitivity at depths between 600 and 1500 km, while the sensitivity of the fundamental-mode surface wave is mostly confined in the top 200 km. In general, Love waves are more sensitive to perturbations in horizontally polarized shear wave speed (β_H) than to perturbations in vertically polarized shear wave speed (β_V). The sensitivity to perturbations in β_V is negligible for fundamental-mode measurements but becomes significant for higher-mode measurements. The two sensitivity kernels—$K_\phi^{\beta_\mathrm{H}}$ and $K_\phi^{\beta_\mathrm{V}}$—are complementary to each other, with $K_\phi^{\beta_\mathrm{V}}$ concentrated at shallower depths compared to $K_\phi^{\beta_\mathrm{H}}$. Love waves are purely associated with shear waves and have no sensitivity to perturbations in

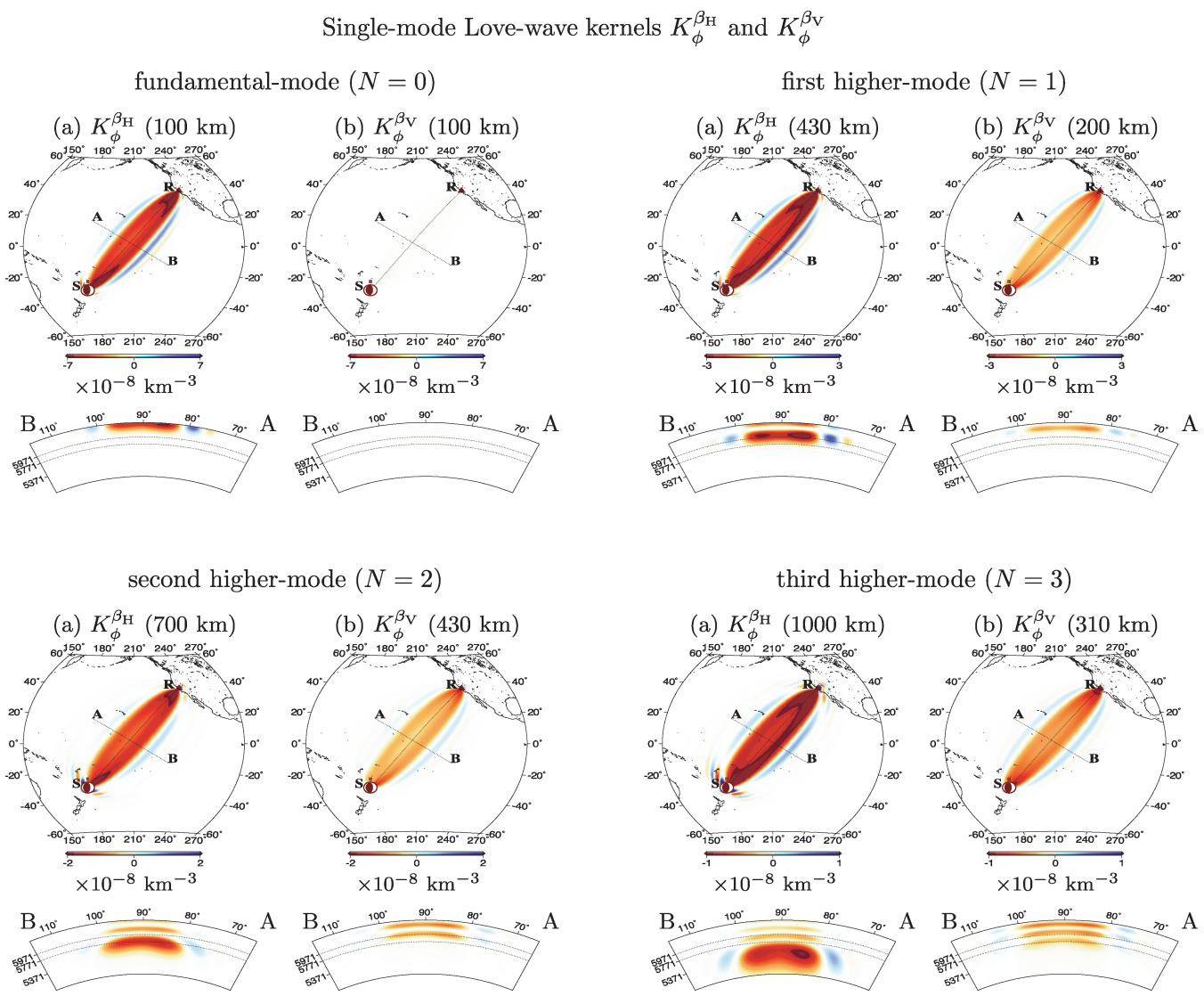

Figure 1. Single-mode Love-wave sensitivity kernels $K_\phi^{\beta_H}$ and $K_\phi^{\beta_V}$, expressing the sensitivity of phase delays to model perturbations in β_H and β_V. The depths at which the mapviews are plotted are indicated in the subtitles; the AB depth cross-sections are plotted half-way between the source (S) and the receiver (R), the dotted lines in the cross-sections are plotted at depths of 400 km and 660 km. Kernels are computed for 10-mHz phase-delay measurements of fundamental-mode ($N = 0$) and the first three higher-mode ($N = 1, 2, 3$) Love waves made with three $3 - \pi$ Slepian multitaper. The length of the measurement window is 800 s for the fundamental mode and 500 s for the overtones, all centred at the group arrival of the corresponding mode. The source–receiver epicentral distance is $\Delta \approx 80^\circ$. The depth of the earthquake is 14 km, and the source mechanism is indicated by the beachball. Mode coupling has been ignored ($\sigma' = \sigma'' = \sigma$) in single-mode calculations. The reference earth model is anisotropic PREM. Fundamental-mode Love waves have little sensitivity to perturbations in β_V, and the sensitivity becomes more significant for overtone modes but mostly confined at relatively shallow depths. In general, the width of the Fresnel zone increases with depth, as seen in the AB depth cross-sections, especially for higher modes.

compressional wave speeds (α_H and α_V) or the intermediate wave speed η.

In the mapviews in Fig. 1, higher-order surface wave modes are associated broader sensitivity than lower-order surface wave modes, mainly due to their faster propagation speed (group velocity). In regions bounded by the first zero-sensitivity ellipse around the great circle path, lateral heterogeneities generate scattered waves interfere constructively with the reference wave. The first surface wave Fresnel zone can be defined as

$$k(\Delta' + \Delta'' - \Delta) + \pi/4 \leq \pi, \tag{30}$$

where the difference in phase between the scattered wave and the reference wave is within half cycle (π). This is different from the definition of 'Fresnel zone' for body waves: the additional $\pi/4$ phase shift in eq. (30) is due to the static phase delay of scattered surface waves upon leaving the secondary source (scatterers)—reflecting a 2-D propagation nature of single-mode surface waves.

The AB depth cross-sections in Fig. 1 show that the width of the Fresnel zone increases with depths, especially for higher-order modes (e.g. $N = 2, 3$.). To make the depth variation in kernel geometry more visible, cross-path sensitivity profiles at different depths are compared in Fig. 2. The sensitivity profiles have been scaled to highlight variations in geometry. The increase in the width of the Fresnel zone with depth is mainly due to frequency averaging introduced by limited timelength of the measurement window. It is not surprising that the sensitivity in the deepest regions is

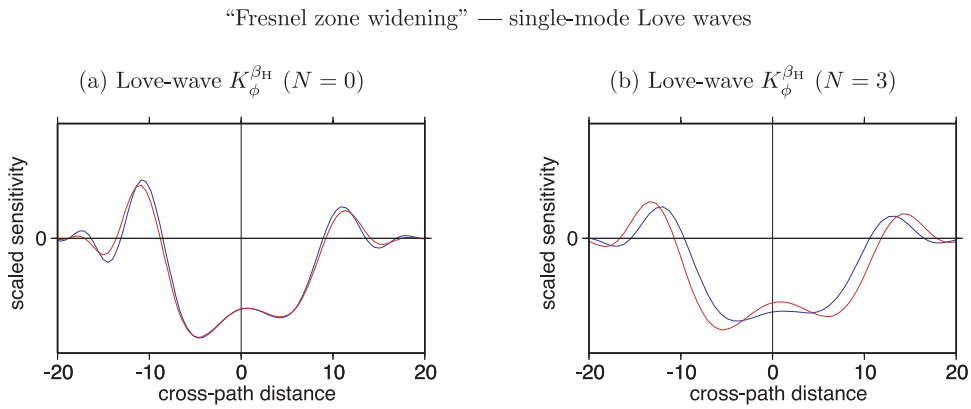

Figure 2. Panel(a) cross-path profiles at depths of 40 km (blue) and 310 km (red) of the AB depth cross-section of the fundamental-mode ($N = 0$) Love-wave kernel $K_\phi^{\beta_H}$ in Fig. 1. Panel(b) cross-path profiles at depths of 430 km (blue) and 1000 km (red) of the AB depth cross-section of the third higher-mode ($N = 3$) Love-wave kernel $K_\phi^{\beta_H}$ in Fig. 1. The cross-path profiles have been normalized to highlight variations in kernel geometry with depth. Overall, the width of the Fresnel zone increases with depth, especially for the overtone mode.

determined by the longest-period signals in the measurement window, leading to Fresnel zone 'widening' with increasing depth. The 'Fresnel zone widening' effects are more significant for higher-mode surface waves than for fundamental-mode surface waves due to the more dispersive nature of overtone modes.

The sensitivity kernels shown in Fig. 1 are not symmetric with respect to the ray path, simply because source radiation is not symmetric with respect to the great circle ray path. The source mechanism for this event is indicated by the beach ball at the source. In general, source radiation pattern depends upon the source mechanism, the source–receiver geometrical configuration, the mode order as well as the frequency of the surface wave.

5.2 Rayleigh-wave single-mode kernels

Examples of sensitivity kernels of single-mode Rayleigh waves, $K_\phi^{\beta_V}$, $K_\phi^{\alpha_H}$, $K_\phi^{\alpha_V}$, K_ϕ^{η}—expressing the sensitivity of phase delays to perturbations in wave speeds β_V, α_H, α_V and η—are plotted in Fig. 3. While Rayleigh-wave sensitivity to perturbations in β_H is negligible and not plotted in Fig. 3, an example of $K_\phi^{\beta_H}$ can be found in Fig. 8. Fig. 3 shows that Rayleigh waves are most sensitive to perturbations in β_V; and, their sensitivity to perturbations in P-wave velocities (α_V and α_H) are mostly confined at shallow depths. Furthermore, the sensitivities of Rayleigh waves to perturbations in α_V and α_H have opposite polarities. In Section 8, I show that Rayleigh-wave sensitivity to isotropic P-wave velocity perturbations is the sum of $K_\phi^{\alpha_V}$ and $K_\phi^{\alpha_H}$; and, due to their opposite polarity, Rayleigh-wave sensitivity to isotropic P-wave velocity perturbations becomes negligible. However, Rayleigh wave sensitivity to P-wave anisotropy (i.e. the difference between α_H and α_V) is significant. Both $K_\phi^{\alpha_H}$ and K_ϕ^{η} are positive within the first Fresnel zone, indicating that an increase in wave speed α_H or η slows down the propagation of Rayleigh waves.

Higher-mode Rayleigh waves show deeper and broader sensitivity compared to fundamental-mode Rayleigh waves; and the coupling between P and S waves also becomes stronger in higher-mode surface waves, as indicated by the stronger overtone sensitivity to P-wave velocity perturbations. In general, the size of the Fresnel zone increases with depth, and significant variations in sensitivity geometry can be identified within the first Fresnel zone as well as in the kernel sidebands, for both fundamental-mode and higher-mode Rayleigh waves (Fig. 4), indicating that single-mode scattering is more a '3-D' feature for Rayleigh waves than for Love waves in this example. The importance of the 3-D nature of fundamental-mode surface waves in seismic tomography have been discussed by Zhou *et al.* (2005).

6 MULTIMODE SENSITIVITY KERNELS

Single-mode sensitivity kernels as shown in Section 5 are often relatively simple in geometry and can be computed very efficiently. In practice, it is difficult to extract a single higher-mode signal from a seismogram as different overtone modes in a narrow frequency band can arrive simultaneously in the seismogram, even at teleseismic distances (Fig. 5). The difficulties have been appreciated by a number of studies trying to utilize the dispersive nature of higher-mode surface waves (overtones) (e.g. Lerner-Lam & Jordan 1983; Nolet 1990; Li & Romanowicz 1996; van Heijst & Woodhouse 1997). In this section, I calculate sensitivity kernels of multimode measurements, accounting for all simultaneous arrivals within the measurement window. Eqs (27)–(29) are used to compute multimode phase-delay and amplitude kernels, and, full mode coupling is taken into account in the computation of both the reference wave (eq. 5) and the scattered wave (eq. 22).

In the following subsections, I compare the geometry of sensitivity kernels computed for single-mode and multimode measurements and show that multimode sensitivity kernels show 'ray-like' features due to coupling among overtone modes. Comparisons will also be made between the sensitivity of phase-delay measurements and amplitude measurements. Most of the discussions in this section are focused on multimode surface wave sensitivities to perturbations in anisotropic wave speeds as well as in density—$K_\phi^{\beta_V}$, $K_\phi^{\alpha_H}$, $K_\phi^{\alpha_V}$, K_ϕ^{η} and K_ϕ^{ρ}; surface wave sensitivity to isotropic velocity perturbations will be address in Section 8. In the final subsections, examples are given to illustrate the dependence of multimode sensitivity upon measurement frequency, wave train as well as windowing and tapering processes applied in making the measurements.

6.1 Phase and amplitude kernels

In Fig. 6, I compare single-mode and multimode sensitivity kernels of both phase-delay and amplitude measurements. In single-mode

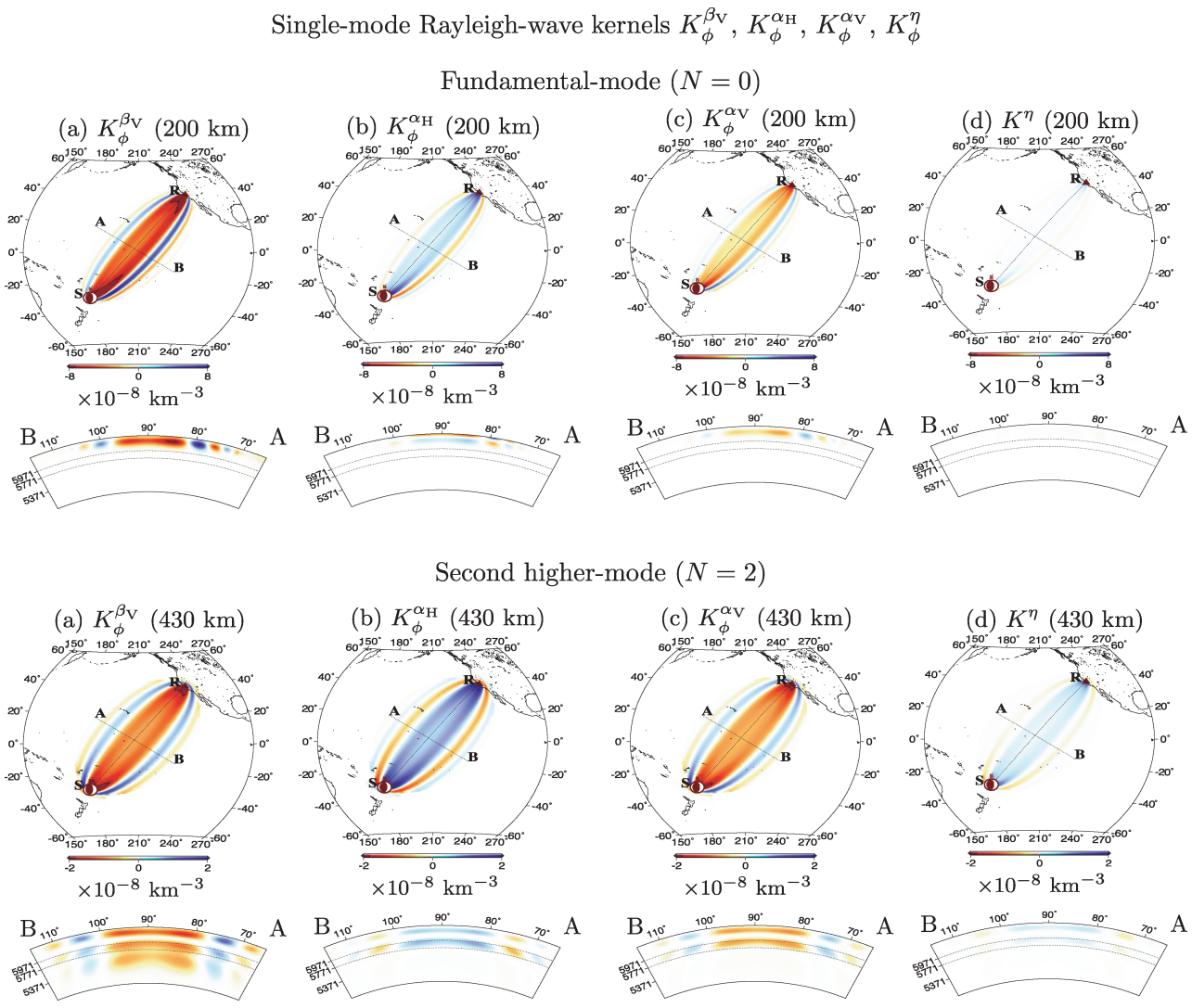

Figure 3. Single-mode Rayleigh-wave sensitivity kernels $K_\phi^{\beta_V}$, $K_\phi^{\alpha_H}$, $K_\phi^{\alpha_V}$, K_ϕ^{η}—expressing the sensitivity of phase delays to model perturbations in β_V, α_H, α_V and η. Rayleigh-wave sensitivity to β_H is negligible and not plotted in this figure but an example is given in Fig. 8. Kernels are computed for 10-mHz phase-delay measurements of fundamental-mode (top panel) as well as the second higher-mode (bottom panel) Rayleigh waves made with three $3 - \pi$ Slepian multitapers, the length of the measurement window is 800 s for the fundamental mode and 300 s for the second higher mode, all centred at the group arrival of the corresponding mode. The source–receiver configuration is the same as in Fig. 1. Note that the overtone mode shows stronger sensitivity to velocity perturbations in α_V and α_H than the fundamental mode, and that $K_\phi^{\alpha_H}$ and $K_\phi^{\alpha_V}$ are mostly confined at shallow depths and have opposite polarities. The size of the Fresnel zone increases with depth, as seen in the AB depth cross-sections, especially for the higher mode.

calculations, only the second higher-mode surface waves ($N = 2$) are accounted for in computing both the reference wave and the scattered wave. In multimode calculations, I account for full mode summation (coupling) in computing both the reference wavefield and the scattered wavefield. The sensitivity kernels in Fig. 6 are computed for multitaper measurements made with three $3 - \pi$ Slepian tapers with a 500-s window centred at the group arrival of the second Love-wave overtone.

The amplitude kernel of the single-mode measurement in Fig. 6 shows a 'narrower' region of negative sensitivity around the great-circle path and stronger sidebands of positive sensitivity, compared to its corresponding phase-delay kernel. This is consistent with the characteristics of fundamental-mode amplitude kernels in isotropic media (Zhou *et al.* 2004). In high-frequency limit (ray theory), phase delays are sensitivity to velocity perturbations along the ray, while amplitudes are sensitive to the second derivative of the velocity perturbation (Woodhouse & Wong 1986; Zhou *et al.* 2004). The mapviews and AB depth cross-sections in Fig. 6 show that the size of the Fresnel zone is roughly the same in the single-mode and multimode kernels, indicating that the second overtone ($N = 2$) is the most energetic mode within the measurement window in this example.

The mapviews and depth profiles along the great-circle path show that the sensitivity of multimode measurements can be very different from that of single-mode measurements. Unlike single-mode kernels, the sensitivity of multimode measurements is no longer negative everywhere along the ray path. This reflects a more '3-D' nature of multimode surface waves: an anomaly along the geometrical ray path can cause either a phase delay or a phase advance, depending upon the depth of the anomaly. In the single-mode case, the along-ray-path profiles show single-mode energy propagating from the source to the receiver (Fig. 6c); while in the case of

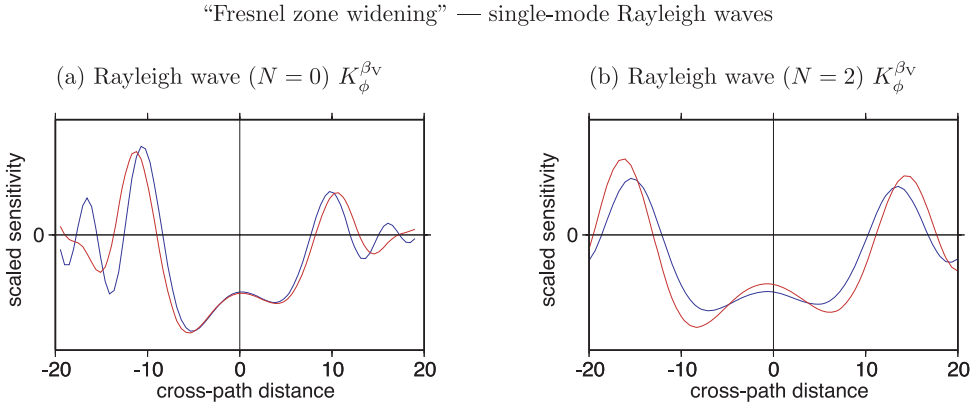

Figure 4. Panel(a) cross-path profiles at depths of 40 km (blue) and 310 km (red) of the AB depth cross-section of the fundamental-mode ($N = 0$) Rayleigh-wave kernel $K_\phi^{\beta_V}$ in Fig. 3. Panel(b) cross-path profiles at depths of 430 km (blue) and 1000 km (red) of the AB depth cross-section of the second higher-mode ($N = 2$) Rayleigh-wave kernel $K_\phi^{\beta_V}$ in Fig. 3 The cross-path profiles have been normalized to highlight variations in kernel geometry with depth. Overall, the width of the Fresnel zone increases with depth, especially for the overtone mode. Note that Rayleigh-wave kernels also show significant depth variations in the sidebands beyond the first Fresnel zone.

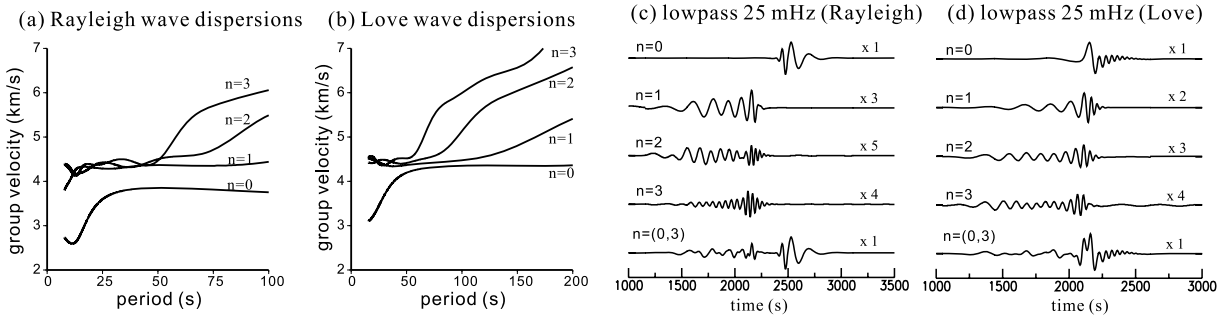

Figure 5. Panels(a) and (b) are group-velocity dispersion curves of fundamental-mode and the first three higher-mode ($n = 0, 1, 2, 3$) Rayleigh waves and Love waves, respectively. Panels(c) are (d) are examples of long-period, single-mode and multimode seismograms. The seismograms are generated for an epicentral distance of ∼80°, and the source–receiver configurations are the same as in Fig. 1. The overtone-mode seismograms have been amplified and the amplification factor is indicated on each seismogram. The multimode seismograms at the bottom of panels(c) and (d) are mode-summed seismograms and the summation is over the first four surface wave modes ($n \leq 3$). Due to strong dispersion, different overtone modes arrive closely in time in the long period seismogram, making it difficult to isolate a single overtone arrival in the mode-summed seismograms. Mode summation over the first four surface wave modes starts to bring out multiple reflected body wave phases. It is worthy noting that full mode summation is required in the calculation of multimode sensitivity kernels.

multimode, interactions between different modes bring out 'body wave' features (Fig. 6e). The phase and amplitude sensitivity kernels of multimode measurements show 'complementary' features: while the phase-delay sensitivity kernel in the source–receiver ray-plane show structures of 'SS' and 'S4' waves, the amplitude measurement made with the same window is most sensitive to perturbations along the 'SSS' ray path. It is worth noting that traveltimes of direct body waves have zero sensitivity along the body wave ray path, while amplitudes have their maximum sensitivity along the ray path (Dahlen *et al.* 2000; Dahlen & Baig 2002; Baig & Dahlen 2004). In Fig. 6, the most energetic modes within the measurement window correspond to 'SSS' waves, therefore, scattered waves generated by heterogeneities right along the ray path of 'SSS' waves will arrive at the same time as the reference wave and therefore affect only the amplitude of the measurement, while scattered waves generated by heterogeneities along the ray path of 'SS' and 'S4' waves arrive either before or after the the reference wave ('SSS' waves), and therefore affect the phase of the measurement. The 'mode-ray duality' of long-period, multimode waves indicates a transition from 2-D propagating surface waves to 3-D multiple-reflected body waves and the 'mode-ray duality' of multimode surface waves will be addressed in Section 9.

6.2 Velocity and density perturbations—$K_\phi^{\beta_V}$, $K_\phi^{\alpha_H}$, $K_\phi^{\alpha_V}$, K_ϕ^{η} and K_ϕ^{ρ}

Fig. 7 shows examples of phase-delay kernels $K_\phi^{\beta_V}$, $K_\phi^{\alpha_H}$, $K_\phi^{\alpha_V}$, K_ϕ^{η} of a multimode Rayleigh-wave measurement at 10 mHz. Sensitivity kernels of single-mode measurement made with the same measurement window are plotted in Fig. 3. In general, Rayleigh-wave sensitivity kernels are more 'messy' compared to those of Love waves due to interactions between *P* waves and *S* waves. The *P*-and-*S* interaction is most significant at shallow depths where Rayleigh waves show strong sensitivity to perturbations in anisotropic *P*-wave velocities (α_H and α_V) as well as the intermediate wave speed η. The sensitivity to *P*-wave speeds, $K_\phi^{\alpha_H}$, and $K_\phi^{\alpha_V}$, are both confined at shallow depths and have opposite polarities. In Section 8, I show that Rayleigh-wave sensitivity to isotropic *P*-wave velocity perturbations—the sum of $K_\phi^{\alpha_H}$ and $K_\phi^{\alpha_V}$—becomes very small due to the opposite polarity of the anisotropic *P*-wave kernels. Overall, Rayleigh waves are most sensitive to vertically polarized *S*-wave speed (β_V), and, the along-ray-path profile of multimode Rayleigh-wave sensitivity $K_\phi^{\beta_V}$ in Fig. 7 indicates that coupling between the overtone modes brings out structures of body waves.

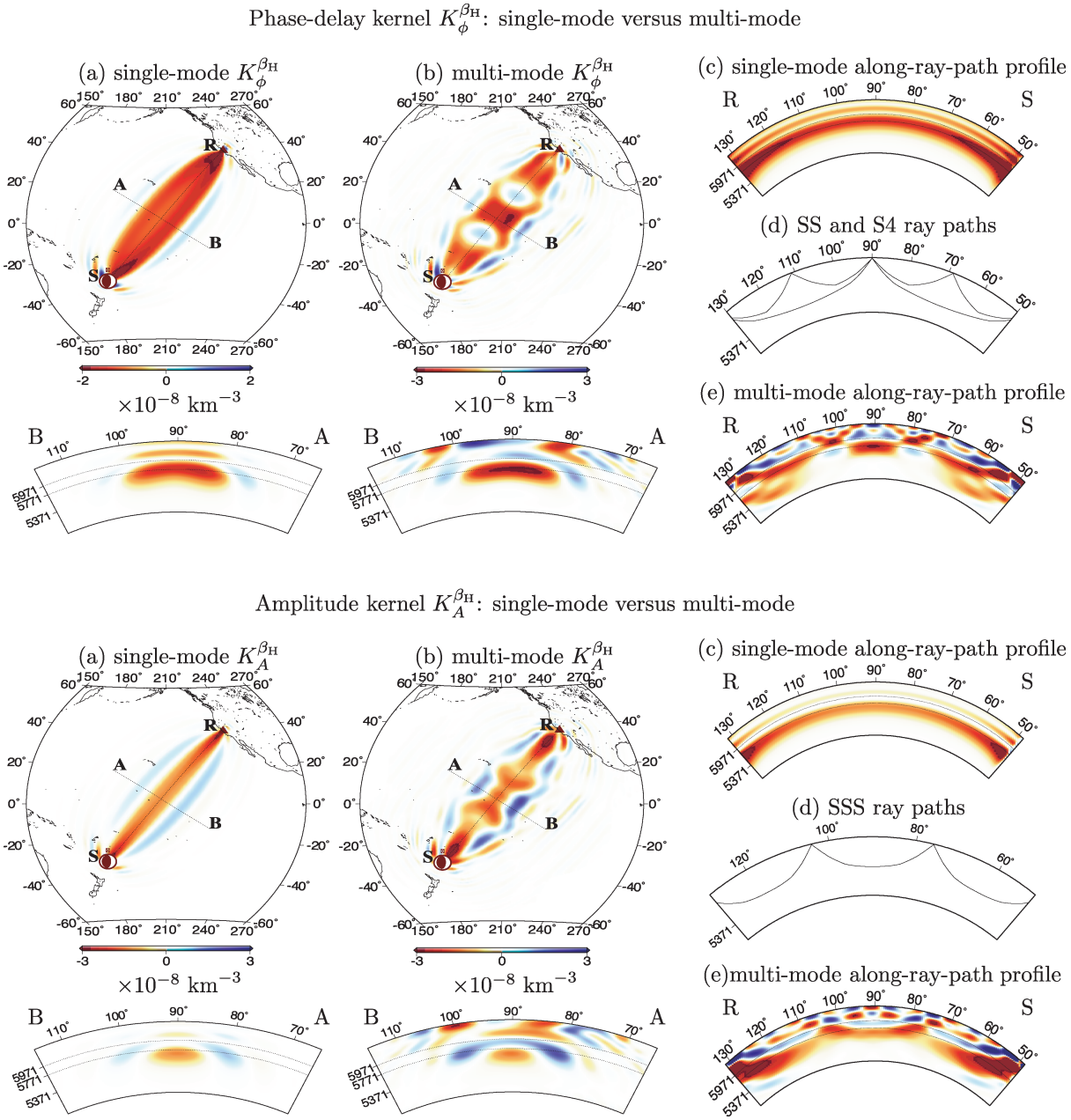

Figure 6. Phase-delay (top panels) and amplitude (bottom panels) kernels of single-mode and multimode Love waves. The source–receiver configurations are the same as in Fig. 1. All mapviews are plotted at 700 km depth. The sensitivity kernels $K_\phi^{\beta_H}$ and $K_A^{\beta_H}$ are calculated for 10-mHz Love-wave phase-delay and amplitude measurements made with three $3-\pi$ Slepian multitapers of 500 s, centred at 1811 s—the group arrival of the second higher-mode ($N=2$) Love wave. In single-mode kernel calculations, only the second higher-mode ($N=2$) Love wave is considered in computing both the reference wave and the scattered wave. In multimode calculations, all surface wave modes are accounted for in computing both the reference wave and the scattered wave. The along-ray-path depth profile of the multimode kernels shows that mode coupling brings out 'body wave' features; and that the multimode phase-delay and amplitude kernels are 'complementary' in sensitivity: while the phase-delay kernel shows structures of 'SS' and 'S4' waves, the amplitude kernel shows mainly features of 'SSS' waves.

Examples of phase-delay sensitivity to perturbations in density (ρ) and *SH*-wave speed (β_H) are plotted in Fig. 8. In general, the sensitivity of Rayleigh waves to perturbations in density is much weaker than the sensitivity to perturbations in *SV* wave speed (Fig. 7). The density kernel (K_ϕ^ρ) of the Rayleigh-wave overtone mode shows polarity variations with depth, consistent with the sensitivity of fundamental-mode surface waves in isotropic media (Zhou *et al.* 2004). The geometry of the multimode Rayleigh-wave density kernel becomes more complex compared to the single-mode kernel, and varies greatly along the great-circle ray path. The sensitivity of Rayleigh waves to perturbations in *SH*-wave speed is about an order of magnitude smaller than the sensitivity to *SV*-wave speed perturbations (i.e. $K_\phi^{\beta_H} << K_\phi^{\beta_V}$), except for off-ray regions in the case of multimode measurements. This indicates that Rayleigh-wave motion in radially anisotropic media is mostly in the source–receiver ray-plane except for off-ray scattered waves when Love-Rayleigh cross-branch mode coupling becomes significant. The effects of cross-branch mode coupling on off-ray surface wave sensitivities

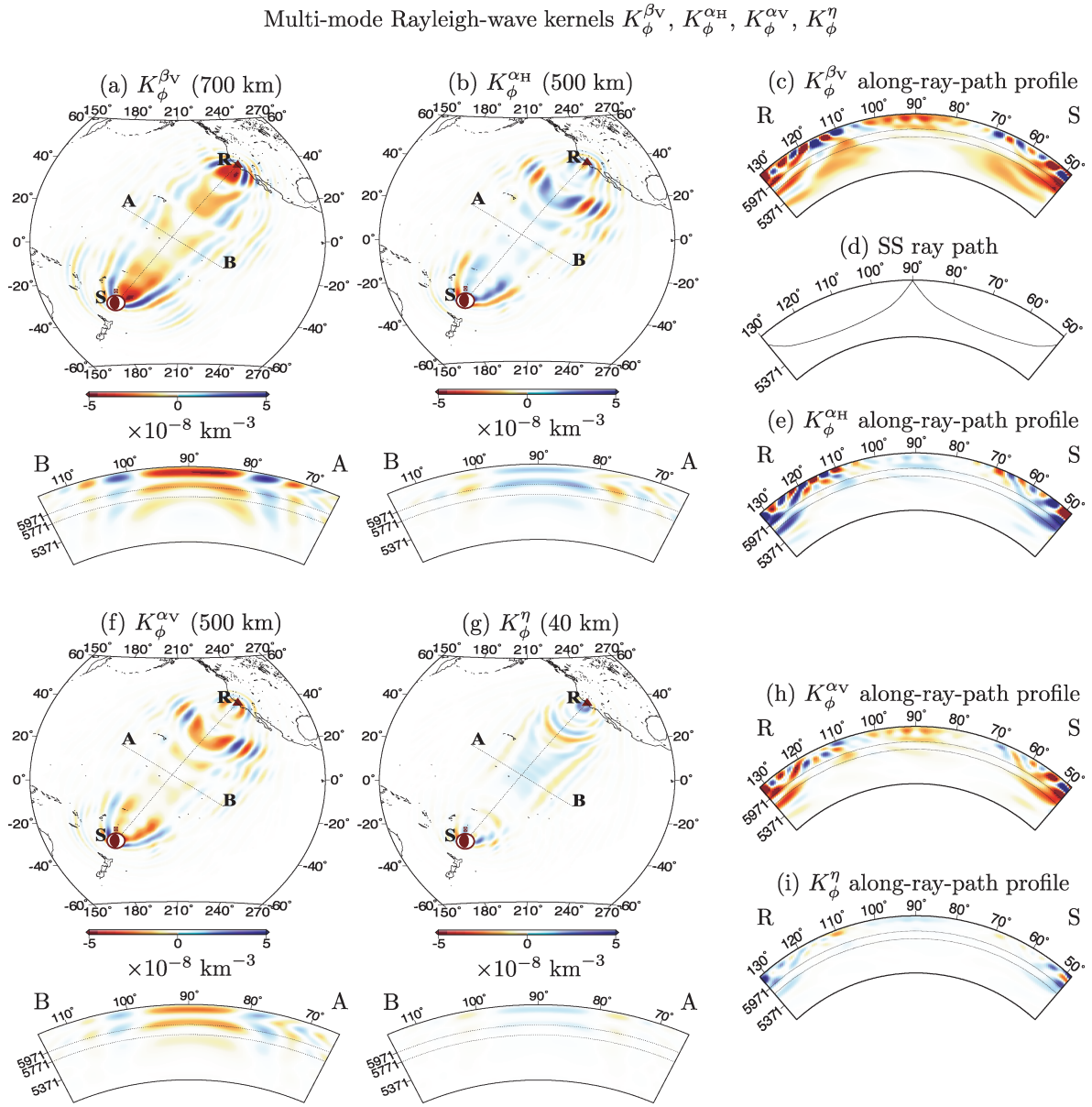

Figure 7. Multimode Rayleigh-wave kernels $K_\phi^{\beta_V}$, $K_\phi^{\alpha_H}$, $K_\phi^{\alpha_V}$ and K_ϕ^{η} for a 10-mHz phase-delay measurement made with three Slepian multitapers of 500 s, centred at 1698 s—the group arrival of the second higher-mode Rayleigh wave. All surface wave modes are accounted for in computing both the reference and the scattered wave field. The source–receiver configurations are the same as in Fig. 1. The AB cross-sections show that multimode Rayleigh waves are most sensitive to vertically polarized *S*-wave speed, and the sensitivity kernel $K_\phi^{\beta_V}$ shows structures of 'SS' waves. Compared to the multimode Love-wave kernels in Fig. 6, the 'ray' features in Rayleigh-wave multimode kernels are more complex due to additional interactions between *P* and *S* waves. The sensitivities of multimode Rayleigh waves to *P*-wave speeds α_H and α_V are significant but mostly confined at shallow depths; and the sensitivity kernels $K_\phi^{\alpha_H}$ and $K_\phi^{\alpha_V}$ have opposite polarities. Rayleigh-wave sensitivity to horizontally polarized *S*-wave speed as well as to density perturbations ($K_\phi^{\beta_H}$ and K_ϕ^{ρ}) are plotted in Fig. 8.

have been noted in previous studies (e.g. Zhou *et al.* 2004; Sieminski *et al.* 2007; Panning & Nolet 2008). The colour scale used in Fig. 8 is the same as in Fig. 3 (but different from that in Fig. 7) to make the relatively weaker sensitivity kernels (K_ϕ^{ρ} and $K_\phi^{\beta_H}$) more visible.

6.3 Major-arc multimode kernels

In global surface wave tomography, phase-delay and amplitude measurements are often made on major-arc wave trains in addition to minor-arc paths to improve the geographical coverage of seismic data. Due to the spherical geometry of the Earth, the antipodes of the source and the receiver play a critical role in surface wave propagation. Fig. 9 shows sensitivity kernels $K_\phi^{\beta_H}(\mathbf{x}, \omega)$ of major-arc multimode Love-wave (G2) measurements made at 20 and 5 mHz. The measurement window is 300-s, and centred at the group arrival of the first Love-wave overtone at 10 mHz. Bandpass filtered major-arc synthetics seismograms are plotted in Fig. 10, where the measurement window is indicated by the shaded box. The mapview of the sensitivity kernels resembles a sausage link, with 'pinches' at the source- and receiver- antipodes (AS and AR). This antipodal 'pinching' has been noted in single-mode surface wave studies (Wang & Dahlen 1995; Spetzler *et al.* 2002; Zhou *et al.* 2004). In the case of multimode measurements, the geometry of the sensitivity can change

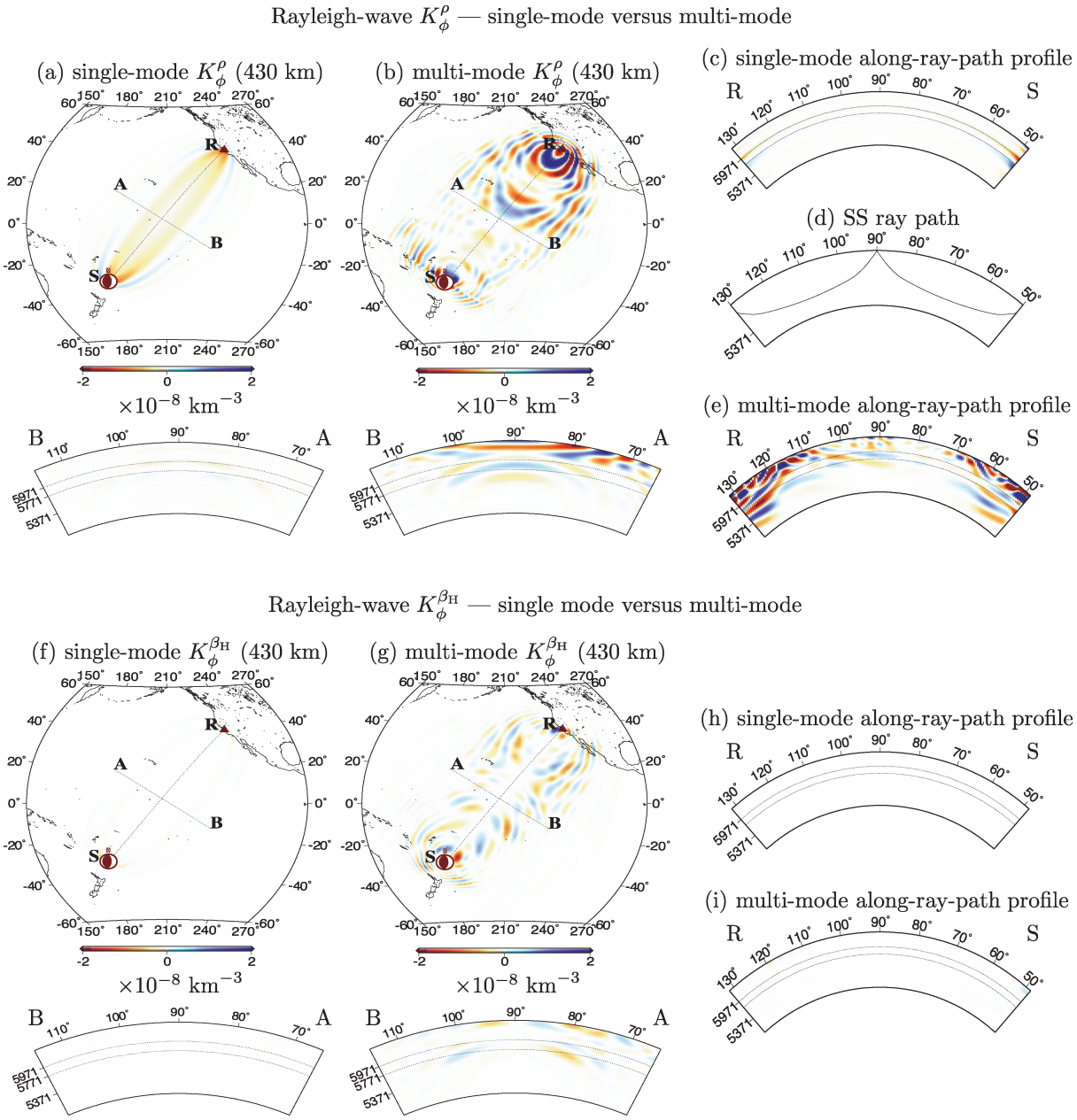

Figure 8. Rayleigh-wave sensitivity kernels K_ϕ^ρ (top panels) and $K_\phi^{\beta_H}$ (bottom panels)—expressing the sensitivity of phase delays to perturbations in density (ρ) and horizontally polarized *S*-wave speed (β_H). The sensitivity kernels are the same as in Figs 3 and 7 except that they are for perturbations in density and *SH*-wave speed. The single-mode density kernel (K_ϕ^ρ) changes its polarity with depth; the corresponding multimode kernel shows more complex structure and the geometry of the kernel varies along the great-circle path. In general, the sensitivity of Rayleigh waves to *SH*-wave speed perturbations ($K_\phi^{\beta_H}$) is negligible, except for off-ray regions in the case of significant Love-Rayleigh cross-branch mode coupling. All sensitivity kernels are plotted on the same colour scale as in Fig. 3 but different from that in Fig. 7.

dramatically upon crossing the antipodes, including polarity changes. For example, the sensitivity of the 20-mHz Love wave changes polarity from positive in the source (S) to receiver-antipode (AR) segment to negative in the receiver-antipode (AR) to source-antipode (AS) segment. This is due to a $\pi/2$ phase shift upon waves crossing the antipodes, leading to different mode interaction patterns at different sides of the antipodes. The effects of the antipode-$\pi/2$ phase shift on mode coupling vary with frequency, as seen from the kernel geometry of the 20- and 5-mHz measurements. The great-circle depth profiles of the major-arc Love wave sensitivity kernels show structures of multiple-reflected *S* waves. Note that measurements at 5 mHz do not show deeper sensitivity than at 20 mHz, this is different from single-mode kernels where longer period measurements correspond to deeper sensitivity. The fact that longer period measurements do not show deeper sensitivity in a multimode system indicate that energy-dominant modes within the measurement window varies with frequency.

Examples of Rayleigh-wave, major-arc, phase-delay sensitivity kernels are plotted in Fig. 11 for measurements made at 10 and 20 mHz. The measurement window is centred at the group arrival of the first higher-mode ($N = 1$) Rayleigh wave at 10 mHz. In this calculation, source and receiver configurations are the same as

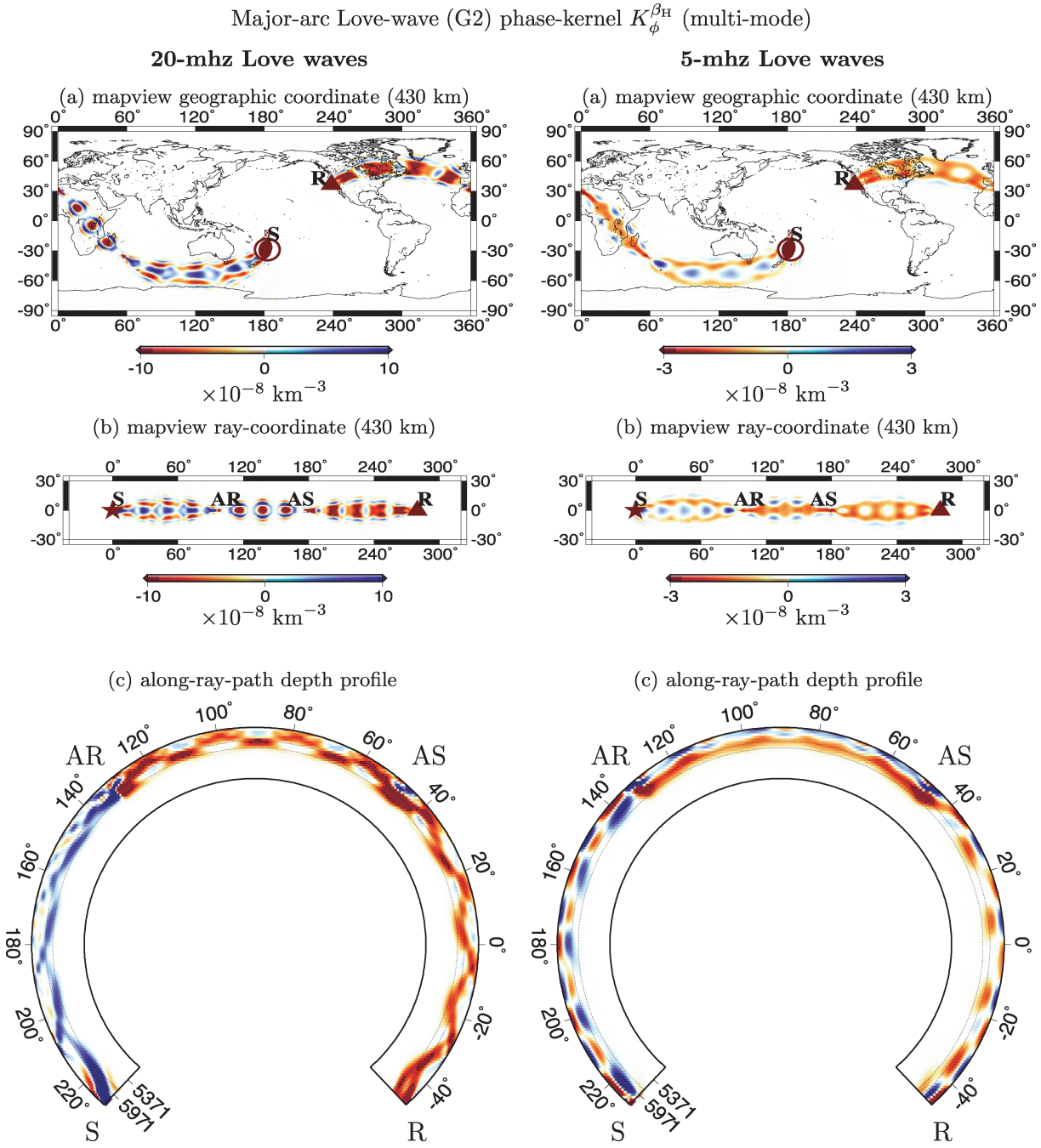

Figure 9. Examples of multimode sensitivity kernels of major-arc Love-wave (G2) phase-delay measurements at 20 mHz (left-hand panels) and 5 mHz (right-hand panels), respectively. The source and receiver configurations are the same as in Fig. 1. Sensitivity kernels are computed for phase delays measured with three $3 - \pi$ Slepian multitapers of 300 s, centred at the group arrival of the first higher-mode Love wave at 10 mHz. Measurement windows as well as bandpass filtered reference seismograms are plotted in Fig. 10. In map views, the sensitivity resembles a sausage link, with 'pinches'' at the source and receiver antipodes (AS and AR). The geometry of the sensitivity kernels changes upon crossing the antipodes (AS and AR), including polarity changes. This is due to a $\pi/2$ phase shift upon waves crossing the antipodes, leading to different mode interaction patterns at different sides of the antipodes. The great-circle depth profiles show a rough correspondence between the major-arc sensitivity kernels and multiple-reflected *S* waves. Unlike simple-mode kernels, measurements at 5 mHz do not show deeper sensitivity than measurements at 20 mHz, indicating that the most energetic modes within the measurement window vary with frequency.

in Fig. 1 except for that the source is located at 300 km depth to avoid weak (nodal) source excitations in the great circle direction at low frequencies. At 10 mHz, the depth profile shows clear polarity changes upon crossing both the source- and the receiver-antipodes (AS and AR). This apparent polarity change is not seen at 20 mHz. The polarity differences in sensitivity between 10 and 20 mHz indicate that energy-dominant modes within measurement window varies with frequency. It is worth pointing out that a polarity change upon crossing the antipode is possible but not necessary for all major-arc kernels, it depends on epicentral distance, measurement

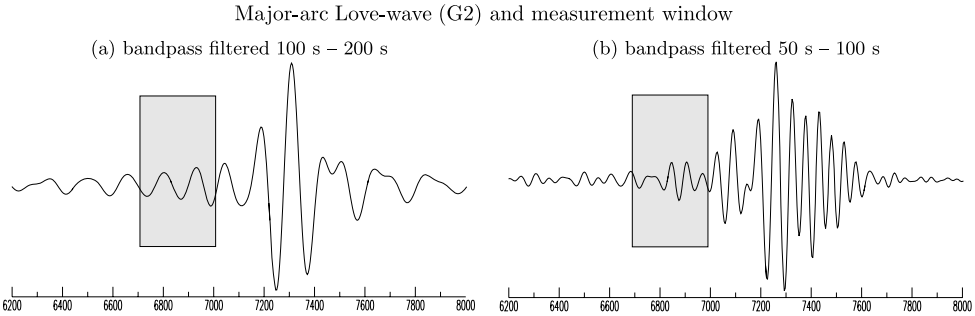

Figure 10. Bandpass-filtered transverse-component seismogram of a major-arc Love wave (G2) in the reference earth model. The length of shaded time window is 300 s, centred at the group arrival of the first higher-mode Love wave at 10 mHz. Sensitivity kernels of multitaper phase-delay measurements made with the shaded time window are plotted in Fig. 9. The source–receiver configurations are the same as in Fig. 1.

frequency, seismogram windowing as well as tapering techniques applied in making the measurements. The example sensitivity kernels shown in Figs 9 and 11 illustrate only a few of many possible kernel geometries.

In the calculation of major-arc sensitivity kernels, backscattered waves in the vicinity of the source- and receiver-antipodes have been neglected. In small regions close to the antipodes, backscattered waves may arrive within the measurement window. It has been suggested that the effects of those scattered wave are relatively small (Zhou *et al.* 2004). Therefore, only the most great-circle-like path is considered at each scatterer in the calculation of scattered wavefield.

6.4 Frequency dependence of multimode kernels

Examples of multimode Love-wave sensitivity kernels are plotted in Fig. 12. The sensitivity kernels are calculated for phase delays at 5 and 20 mHz. The source and receiver configurations are the same as in Fig. 1 except for that the source is located at a depth of 350 km such that there is preferred source excitation of higher-mode surface waves. The mapviews and AB depth cross-sections show a wider-but-not-deeper sensitivity region in the long-period (5 mHz) sensitivity kernel compared to the short-period (20 mHz) sensitivity kernel. The along-ray-path profiles show that both sensitivity kernels roughly correspond to the ray path of 'S4' waves, and, long-period waves do not show deeper sensitivity than short-period waves—this is consistent with observations made on major-arc Love waves (Fig. 9). Unlike single-mode kernels, the depth extent of multimode surface wave sensitivity is determined by the coupling among surface wave modes.

6.5 Windowing and tapering effects

In Fig. 13, I compare Love-wave sensitivity kernels of 15-mHz phase-delay measurements made with two different measurement windows: window I is centred at the group arrival of the first overtone mode at 10 mHz and window II is centred at the group arrival of the second overtone mode at 10 mHz. The sensitivity kernels of the measurement made with Window I show structures of 'S4' waves as well as fundamental-mode surface waves as the measurement window picks up late-arriving modes. Window II picks up early-arriving overtone modes and the corresponding sensitivity kernel shows structures of 'SS' and 'S4' waves. The effects of seismogram tapering on phase-delay sensitivity kernels are illustrated in Fig. 14, where sensitivity kernels are plotted for measurements made with the same measurement window but using different tapering technique: Slepian multitaper, box-car taper and cosine taper (Fig. 14). The phase-delay sensitivity kernels differ greatly for measurements made with different tapering technique: the multitaper sensitivity kernel shows a rough correspondence to 'SS' and 'S4' waves; the sensitivity kernel of the boxcar measurement show strong sensitivity towards the surface of the earth, indicating some fundamental-mode energy within the measurement window; while the sensitivity kernel of the cosine-taper measurement shows mainly structures of 'SS' waves.

7 SINGLE-MODE REDUCTION: 2-D SENSITIVITY KERNELS AND RAY THEORY

Following Zhou *et al.* (2004), I show in this section that for single-mode measurement, the 3-D sensitivity to wave speed perturbations in $\alpha_{\rm H}$, $\alpha_{\rm V}$, $\beta_{\rm H}$, $\beta_{\rm V}$ and η and density ρ can be combined to find the 2-D sensitivity to the local phase-velocity perturbation, $\delta c/c$, using a forward-scattering approximation. The 2-D phase-delay and amplitude sensitivity kernels $K^c_\phi(\hat{\mathbf{r}}, \omega)$ and $K^c_A(\hat{\mathbf{r}}, \omega)$ are defined as

$$\begin{aligned}\delta\phi(\omega) &= \iint_\Omega K^c_\phi(\hat{\mathbf{r}}, \omega)\left(\frac{\delta c}{c}\right)\mathrm{d}\Omega,\\ \delta \ln \mathcal{A}(\omega) &= \iint_\Omega K^c_A(\hat{\mathbf{r}}, \omega)\left(\frac{\delta c}{c}\right)\mathrm{d}\Omega,\end{aligned} \tag{31}$$

where the integration is over the unit sphere $\Omega = \{\hat{\mathbf{r}} : ||\hat{\mathbf{r}}||^2 = 1\}$. Upon neglecting mode coupling effects (i.e. assuming that $\sigma' = \sigma'' = \sigma$), the only depth dependent term in eqs (26)–(29) is the scattering coefficient ${}_{\sigma'}\Omega^m_{\sigma''}$ implied in the waveform kernel $\mathcal{K}^m(\mathbf{x}, \omega)$ (eq. 22) and the model perturbation δm. The depth integration in eq. (26) reduces to local phase-velocity perturbation ($\delta c/c$) upon applying a paraxial forward-scattering approximation (i.e. the scattering angle $\psi = \arccos(\mathbf{k}' \cdot \mathbf{k}'') = 0$):

$$\begin{aligned}&\int_0^a \left[{}_{\sigma'}\Omega^{\alpha_{\rm H}}_{\sigma''}\left(\frac{\delta\alpha_{\rm H}}{\alpha_{\rm H}}\right) + {}_{\sigma'}\Omega^{\alpha_{\rm V}}_{\sigma''}\left(\frac{\delta\alpha_{\rm V}}{\alpha_{\rm V}}\right) + {}_{\sigma'}\Omega^{\beta_{\rm V}}_{\sigma''}\left(\frac{\delta\beta_{\rm V}}{\beta_{\rm V}}\right)\right] r^2\,\mathrm{d}r\\ &+ \int_0^a \left[{}_{\sigma'}\Omega^{\beta_{\rm H}}_{\sigma''}\left(\frac{\delta\beta_{\rm H}}{\beta_{\rm H}}\right) + {}_{\sigma'}\Omega^{\eta}_{\sigma''}\left(\frac{\delta\eta}{\eta}\right) + {}_{\sigma'}\Omega^{\rho}_{\sigma''}\left(\frac{\delta\rho}{\rho}\right)\right] r^2\,\mathrm{d}r\\ &= -2k^2\left(\frac{\delta c}{c}\right),\end{aligned} \tag{32}$$

where $c = \omega/k$ is the phase velocity measured in rad s^{-1}, and $\delta c(\hat{\mathbf{r}}, \omega)$ is the associated local perturbation in phase velocity. The above analytical expression of the depth integration can be applied to reduce the the 3-D integration in eq. (26) to 2-D, leading to 2-D multitaper sensitivity kernels. In the case of single-frequency waves,

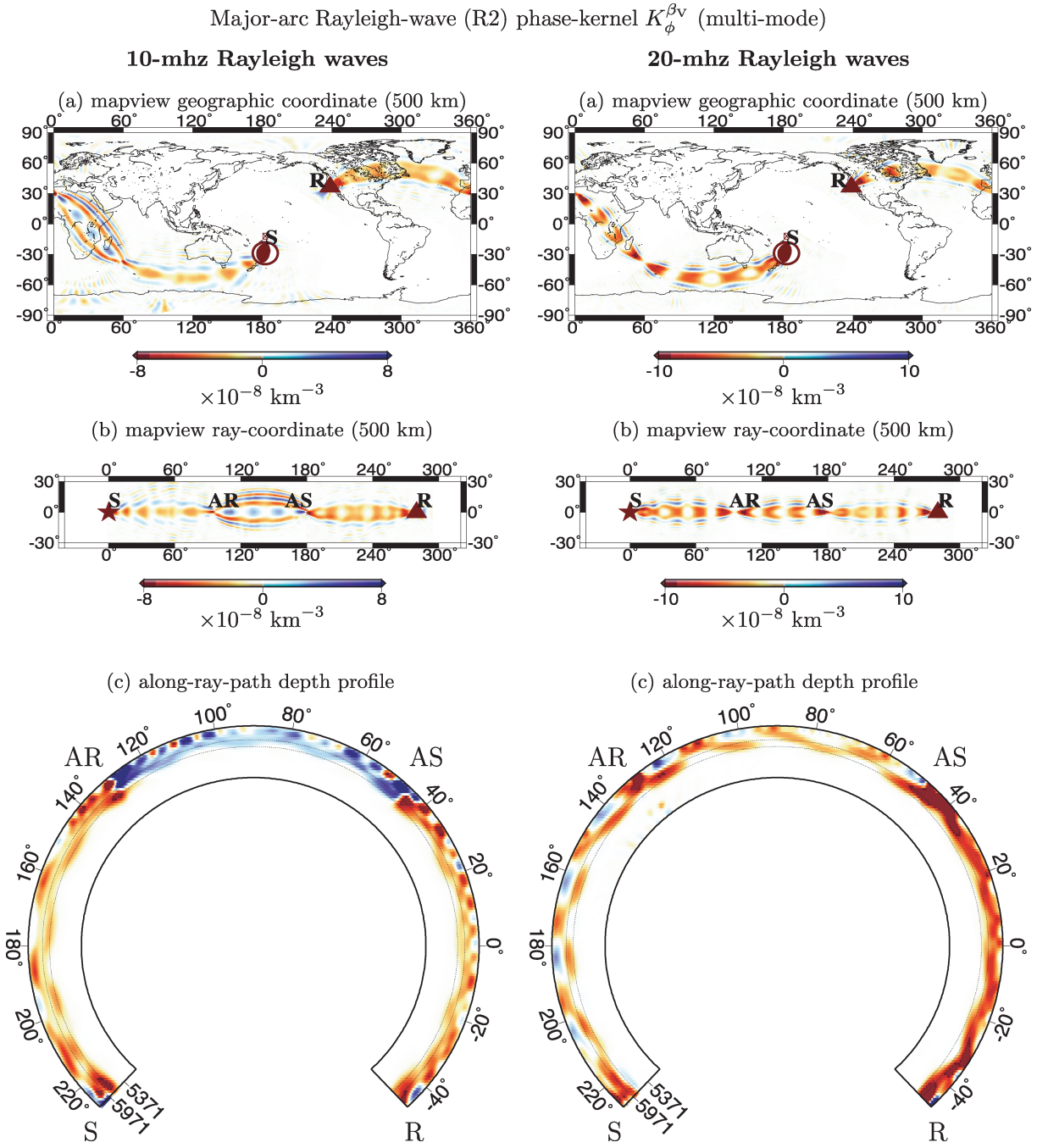

Figure 11. Examples of multimode sensitivity kernels of major-arc Rayleigh-wave (R2) phase-delay measurements at 10 mHz (left-hand panels) and 20 mHz (right-hand panels), respectively. The source and receiver configurations are the same as in Fig. 1 except for that the source is located at 300 km depth in this calculation. At 10 mHz, the along-ray-path depth profile shows that the polarity of the sensitivity kernel changes upon crossing the antipodes (AS and AR). This is due to a $\pi/2$ phase shift upon waves crossing the antipodes, leading to different mode interaction patterns at different sides of the antipodes. This apparent polarity change upon crossing the antipodes is not seen at 20 mHz. The depth profiles show a rough correspondence between the major-arc sensitivity kernels and multiple-reflected S waves; and, measurements at 10 mHz do not show deeper sensitivity than at 20 mHz, indicating that the most energetic modes within the measurement window vary with frequency. The sensitivity kernels are computed for phase delays measured with three $3-\pi$ Slepian multitapers of 500 s, centred at 6911 s—the group arrival of the first higher-mode Rayleigh wave at 10 mHz.

the taper spectra in eqs (27)–(29) reduces to a Dirac delta function, that is, $h(\omega)=\delta(\omega)$, and the 2-D kernels can be expressed as (Zhou *et al.* 2004)

$$K_\phi^c(\hat{\mathbf{r}},\omega) = \mathrm{Im}\left[\frac{2k^2\mathcal{S}'\mathcal{R}''e^{-i\,[k(\Delta'+\Delta''-\Delta)-(n'+n''-n)\pi/2+\pi/4]}}{\mathcal{S}\mathcal{R}\sqrt{8\pi k(|\sin\Delta'||\sin\Delta''|/|\sin\Delta|)}}\right], \quad (33)$$

$$K_A^c(\hat{\mathbf{r}},\omega) = -\mathrm{Re}\left[\frac{2k^2\mathcal{S}'\mathcal{R}''e^{-i\,[k(\Delta'+\Delta''-\Delta)-(n'+n''-n)\pi/2+\pi/4]}}{\mathcal{S}\mathcal{R}\sqrt{8\pi k(|\sin\Delta'||\sin\Delta''|/|\sin\Delta|)}}\right]. \quad (34)$$

Zhou *et al.* (2004) show that the above 2-D finite-frequency sensitivity kernels further reduces to ray theory when model perturbations vary slowly over space and the length scale of lateral heterogeneities

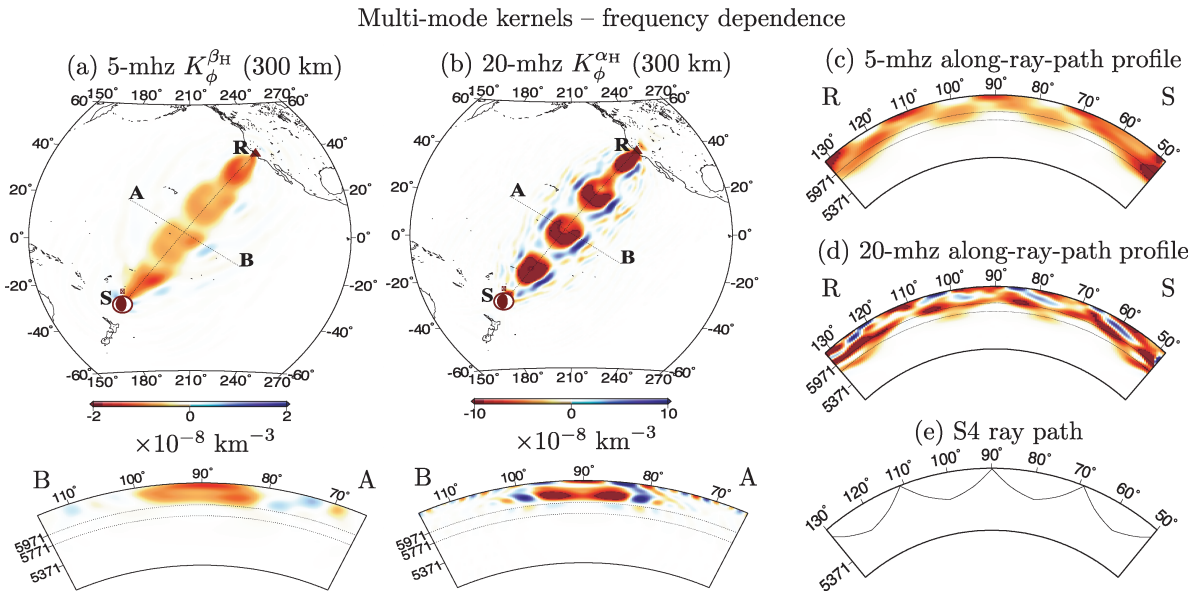

Figure 12. Examples of minor-arc Love-wave sensitivity kernels at 5 and 20 mHz. Sensitivity kernels are computed for phase delays measured with three $3-\pi$ Slepian multitapers of 500 s, centred at 2085 s—the group arrival of the first higher-mode Love wave at 10 mHz. The source and receiver configurations are the same as in Fig. 1 except for that the source is located at a depth of 350 km. The mapviews and AB depth cross-sections show a wider-but-not-deeper sensitivity region in the long-period (5 mHz) sensitivity kernel compared to the short-period (20 mHz) sensitivity kernel. The along-ray-path profiles show that both sensitivity kernels roughly correspond to the ray path of 'S4' waves.

is much larger than the size of the Fresnel zone. It is worth pointing out that the reduction to 2-D kernel and to surface wave ray theory is only possible for single-mode waves. For multimode measurements, the sensitivity is fully 3-D as a result of cross-branch mode coupling.

8 KERNELS FOR ISOTROPIC PERTURBATIONS

In this section, I show that it is straightforward to combine anisotropic sensitivity kernels to obtain sensitivity kernels for isotropic velocity perturbations. In isotropic media,

$$\alpha_H = \alpha_V, \quad \beta_H = \beta_V \quad \text{and } \eta = 1, \tag{35}$$

and,

$$\delta\alpha_H = \delta\alpha_V = \delta\alpha, \quad \delta\beta_H = \delta\beta_V = \delta\beta, \quad \delta\eta = 0. \tag{36}$$

Phase-delay and amplitude measurements ($\delta\phi$ and $\delta \ln \mathcal{A}$) in an isotropic earth model can be written as volumetric integration over perturbations in isotropic wave speeds (α and β) and density (ρ) as

$$\begin{aligned}\delta\phi(\omega) &= \iiint_{\oplus} \left[K_\phi^\alpha(\mathbf{x},\omega)\,\delta\ln\alpha(\mathbf{x}) + K_\phi^\beta(\mathbf{x},\omega)\,\delta\ln\beta(\mathbf{x}) \right. \\ &\qquad \left. + K_\phi^\rho(\mathbf{x},\omega)\,\delta\ln\rho(\mathbf{x}) \right] \mathrm{d}\mathbf{x}^3, \\ \delta\ln A(\omega) &= \iiint_{\oplus} \left[K_A^\alpha(\mathbf{x},\omega)\,\delta\ln\alpha(\mathbf{x}) + K_A^\beta(\mathbf{x},\omega)\,\delta\ln\beta(\mathbf{x}) \right. \\ &\qquad \left. + K_A^\rho(\mathbf{x},\omega)\,\delta\ln\rho(\mathbf{x}) \right] \mathrm{d}\mathbf{x}^3, \end{aligned} \tag{37}$$

where $K^\alpha_{\phi,A}$ and $K^\beta_{\phi,A}$ are the isotropic phase and amplitude sensitivity kernels—representing the sensitivity of phase-delay and amplitude measurements to isotropic P- and S-wave velocity perturbations, respectively. In eq. (26), the product of the scattering coefficients ${}_{\sigma'}\Omega^m_{\sigma''}$ and model perturbation δm in the integration kernel can be re-arranged using eqs (35) and (36),

$$\begin{aligned}{}_{\sigma'}\Omega^m_{\sigma''}\delta m &= {}_{\sigma'}\Omega^{\alpha_H}_{\sigma''}\left(\frac{\delta\alpha_H}{\alpha_H}\right) + {}_{\sigma'}\Omega^{\alpha_V}_{\sigma''}\left(\frac{\delta\alpha_V}{\alpha_V}\right) + {}_{\sigma'}\Omega^{\beta_V}_{\sigma''}\left(\frac{\delta\beta_V}{\beta_V}\right) \\ &\quad + {}_{\sigma'}\Omega^{\beta_H}_{\sigma''}\left(\frac{\delta\beta_H}{\beta_H}\right) + {}_{\sigma'}\Omega^{\eta}_{\sigma''}\left(\frac{\delta\eta}{\eta}\right) + {}_{\sigma'}\Omega^{\rho}_{\sigma''}\left(\frac{\delta\rho}{\rho}\right) \\ &= {}_{\sigma'}\Omega^{\alpha}_{\sigma''}\left(\frac{\delta\alpha}{\alpha}\right) + {}_{\sigma'}\Omega^{\beta}_{\sigma''}\left(\frac{\delta\beta}{\beta}\right) + {}_{\sigma'}\Omega^{\rho}_{\sigma''}\left(\frac{\delta\rho}{\rho}\right), \end{aligned} \tag{38}$$

where ${}_{\sigma'}\Omega^\alpha_{\sigma''}$ and ${}_{\sigma'}\Omega^\beta_{\sigma''}$ are the isotropic scattering coefficients—representing the 'strength' of scattering due to perturbations in wave speeds α and β, and,

$${}_{\sigma'}\Omega^\alpha_{\sigma''} = {}_{\sigma'}\Omega^{\alpha_H}_{\sigma''} + {}_{\sigma'}\Omega^{\alpha_V}_{\sigma''}, \quad {}_{\sigma'}\Omega^\beta_{\sigma''} = {}_{\sigma'}\Omega^{\beta_H}_{\sigma''} + {}_{\sigma'}\Omega^{\beta_V}_{\sigma''}. \tag{39}$$

The linear dependence of the sensitivity kernels upon the scattering coefficients guarantees

$$K^\alpha_{\phi,A} = K^{\alpha_H}_{\phi,A} + K^{\alpha_V}_{\phi,A}, \quad K^\beta_{\phi,A} = K^{\beta_H}_{\phi,A} + K^{\beta_V}_{\phi,A}. \tag{40}$$

Examples of phase-delay sensitivity kernels to anisotropic as well as to isotropic velocity perturbations are plotted in Fig. 15 for single-mode measurements. The sensitivity of phase delays to isotropic S-wave velocity perturbations is the sum of the sensitivity to SH- and SV-velocity perturbations (eq. 40). The sensitivities of Love waves to perturbations in SH- and SV- wave speed are complementary, therefore, Love waves are more sensitive to perturbations in isotropic S-wave velocity (β) than to perturbations in anisotropic S-wave speeds (β_H or β_V). For single-mode Rayleigh waves, phase delays are most sensitive to perturbations in β_V, and the sensitivity to perturbations in β_H is negligible (Fig. 8). The sensitivities of Rayleigh waves to perturbations in α_H and α_V have opposite polarities, as a result, the sensitivity of a single-mode Rayleigh wave to perturbations in isotropic P-wave velocity (α) is very weak and only confined at shallow depths.

Examples of multimode surface wave sensitivity to anisotropic and isotropic velocity perturbations are plotted in Fig. 16. The

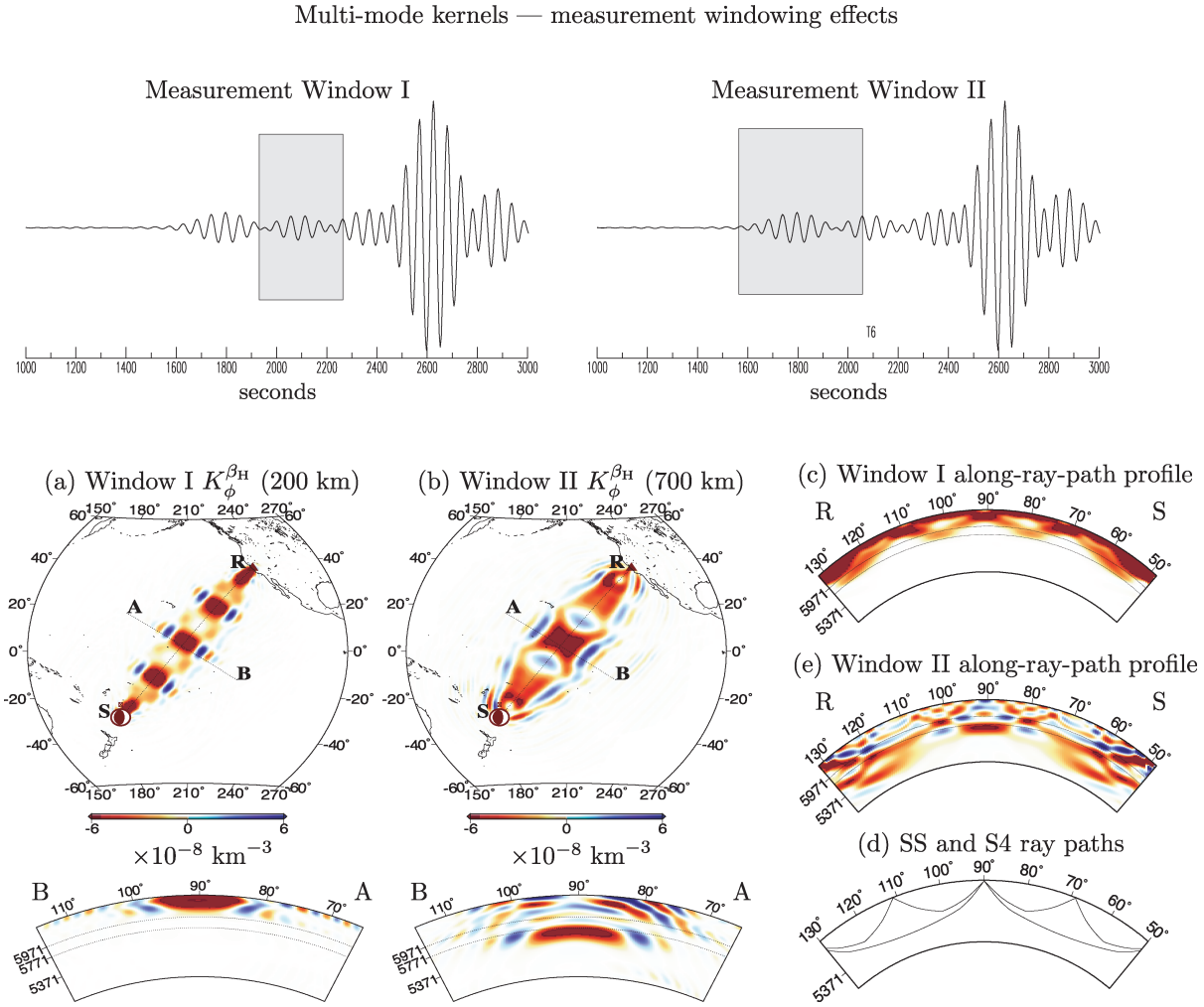

Figure 13. Examples of multimode Love-wave sensitivity kernels ($K_\phi^{\beta_H}$) of 15-mHz phase-delay measurements made with three $3-\pi$ Slepian multitapers applied on two different measurement windows: Window I is 300-s and centred at the group arrival of the first higher-mode Love wave at 10 mHz; and Window II is 500-s and centred at the group arrival of the second higher-mode Love wave at 10 mHz. The seismograms are bandpass filtered between 15 and 20 mHz. The source and receiver configurations are the same as in Fig. 1. The phase-delay kernel of the later arrival (Window I) shows shallower sensitivity and structures of 'S4' waves as well as fundamental-mode surface waves; while the sensitivity kernel of the earlier arrival (Window II) shows deeper sensitivity and structures 'SS' and 'S4' waves.

coupled-mode Love waves show strong sensitivity to *SH*-wave speed perturbations, and, the along-ray-path profile of $K_\phi^{\beta_H}$ show characteristics of 'SS' and 'S4' waves. The sensitivity of multimode Love waves to *SV*-wave speed perturbations is weaker and confined at shallower depths, and, the along-ray-path profile of $K_\phi^{\beta_V}$ shows structure of 'S4' waves. The polarity of the anisotropic sensitivity kernels, $K_\phi^{\beta_H}$ and $K_\phi^{\beta_V}$, is the same; as a result, the isotropic sensitivity kernel K_ϕ^{β} is stronger than the anisotropic kernels ($K_\phi^{\beta_H}$ or $K_\phi^{\beta_V}$). The multimode Rayleigh-wave kernel shown in Fig. 16 confirms the significance of Rayleigh-wave sensitivities to perturbations in anisotropic *P*-wave velocities (α_H and α_V); and, the sensitivity of multimode Rayleigh waves to perturbations in isotropic *P*-wave velocity (α) is much weaker due to the opposite polarity of $K_\phi^{\alpha_H}$ and $K_\phi^{\alpha_V}$. It is worth pointing out that sensitivity kernels in this section (Figs 15 and 16) are computed using an isotropic reference earth model, 1066A (Gilbert & Dziewonski 1975), and the sensitivity kernels do not show strong dependence upon the reference model.

9 MODE-RAY DUALITY AND JEAN'S RELATION

The relation between 'modes' and 'rays' can be quantified using Jean's relation (1927)

$$\omega p = l + 1/2, \tag{41}$$

where ω is the frequency of the wave, l is the angular order of the mode, and p is the ray parameter of the corresponding 'ray'. The dispersion diagram (ω– l) of Love wave modes in anisotropic PREM is plotted in Fig. 17. A suite of modes (ω, l) with a constant ray parameter of $p \approx 915$ s is plotted in a blue line, corresponding to rays turning at ~700 km with a turning point velocity of ~6.2 km s^{-1}. The blue line intercepts with the second higher mode ($N = 2$) at a frequency of ~10 mHz. Examples of sensitivity kernels for measurements made windows centred at the group arrivals of the second higher mode Love wave ($N = 2$) at 10 mHz are plotted in Fig. 18, at epicentral distances of 80°, 100° and 120°. Regardless of the epicentral distances—which correspond to

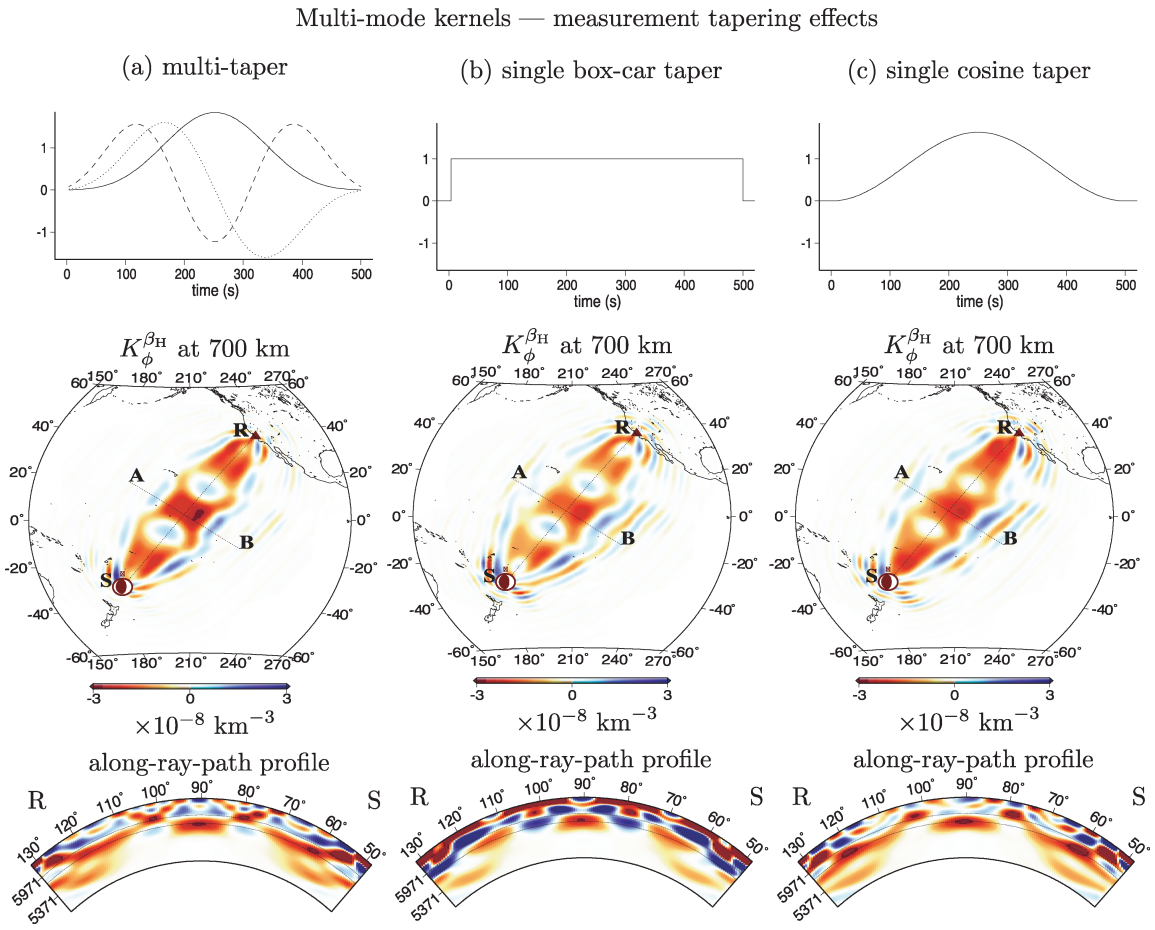

Figure 14. Examples of multimode Love-wave sensitivity kernels ($K_\phi^{\beta_H}$) of 10-mHz phase-delay measurements made with three different tapering techniques: (a) three $3-\pi$ Slepian multitapers, (b) single box-car taper and (c) single cosine taper. All tapers are 500-s in length and centred at 1811 s—the group arrival of the second Love-wave higher mode at 10 mHz. Measurements made with different tapering techniques show significantly different sensitivity to model perturbations: the sensitivity kernel of the multitaper measurement shows rough correspondences to 'SS' and 'S4' waves; the boxcar measurement shows strong sensitivity towards the surface of the earth, indicating fundamental-mode energy picked up by the box-car taper; and the sensitivity kernel of the cosine-taper measurement shows mainly structures of 'SS' waves.

different time windows in seismogram—the maximum sensitivity of the phase-delay measurements are located at around 700 km depth. The along-ray-path profiles show structures of different groups of 'rays' at different epicentral distance: at epicentral distance of $\Delta = 80^\circ$, the sensitivity kernel shows structures of 'SS' and 'S4' waves, while at $\Delta = 120^\circ$, the sensitivity kernel shows clear features of turning 'rays', but does not show apparent correspondence to 'standard' body wave phases.

Jean's relation allows us to associate 'rays' with dispersive 'mode' signals. The turning depth of a body wave 'ray' determines the ray parameter (p), and, the arrival times of this particular 'ray' (measurement window) can be calculated based upon the ray parameter for any given epicentral distance, meanwhile, Jean's relation can be used to determine the suite of surface wave modes (ω, l) associated with the ray parameter. In another word, seismic waves can be viewed as either 'rays' or 'modes', and, a measurement time window at a given epicentral distance is associated the 'turning points' of the 'rays' and the maximum sensitivity depth of the coupled 'modes'. The angular quantization relation (eq. 41) between 'modes' and 'rays' can be used to provide guidelines for measurement window determination to maximize the sensitivity at a target depth range.

The long-period, multimode, surface wave sensitivity kernels in Section 6 show 'ray' characteristics of multiple-reflected body waves; strictly speaking, they are often associated with families of 'rays' instead of a single 'ray' due to the finite length of the measurement window; and, the 'ray' features do not necessary correspond to 'standard' body wave phases. Seismic signals that arrive just before fundamental-mode surface waves travel at a slow speed, and correspond to 'rays' with large ray parameters p (shallow 'turning points') or overtone 'modes' with shallow depth sensitivities. At short period ($< \sim$50 s), low-order, surface wave overtones have similar dispersion properties (Fig. 5), therefore, coupling among overtone modes brings out multiple-reflected body wave 'ray' features that can be stable over the frequency band; furthermore, the number of modes that need to be considered increases with frequency; as a result, short-period signals can be more efficiently analysed as multiple-reflected body waves than coupled modes. At longer period ($> \sim$50 s), the number of overtone modes need to be considered is limited (Fig. 17), moreover, overtone modes are in general more dispersive at longer period and their dispersion curves are further apart (Fig. 5); as a result, the 'ray' features associated with mode coupling show more variations with frequency and the multimode signals are more dispersive. Therefore, long-period waves can be more readily analysed as 'modes' as opposed to 'rays'. The 'mode' nature of longer-period waves can become more significant when there is preferred source excitation of a single overtone mode.

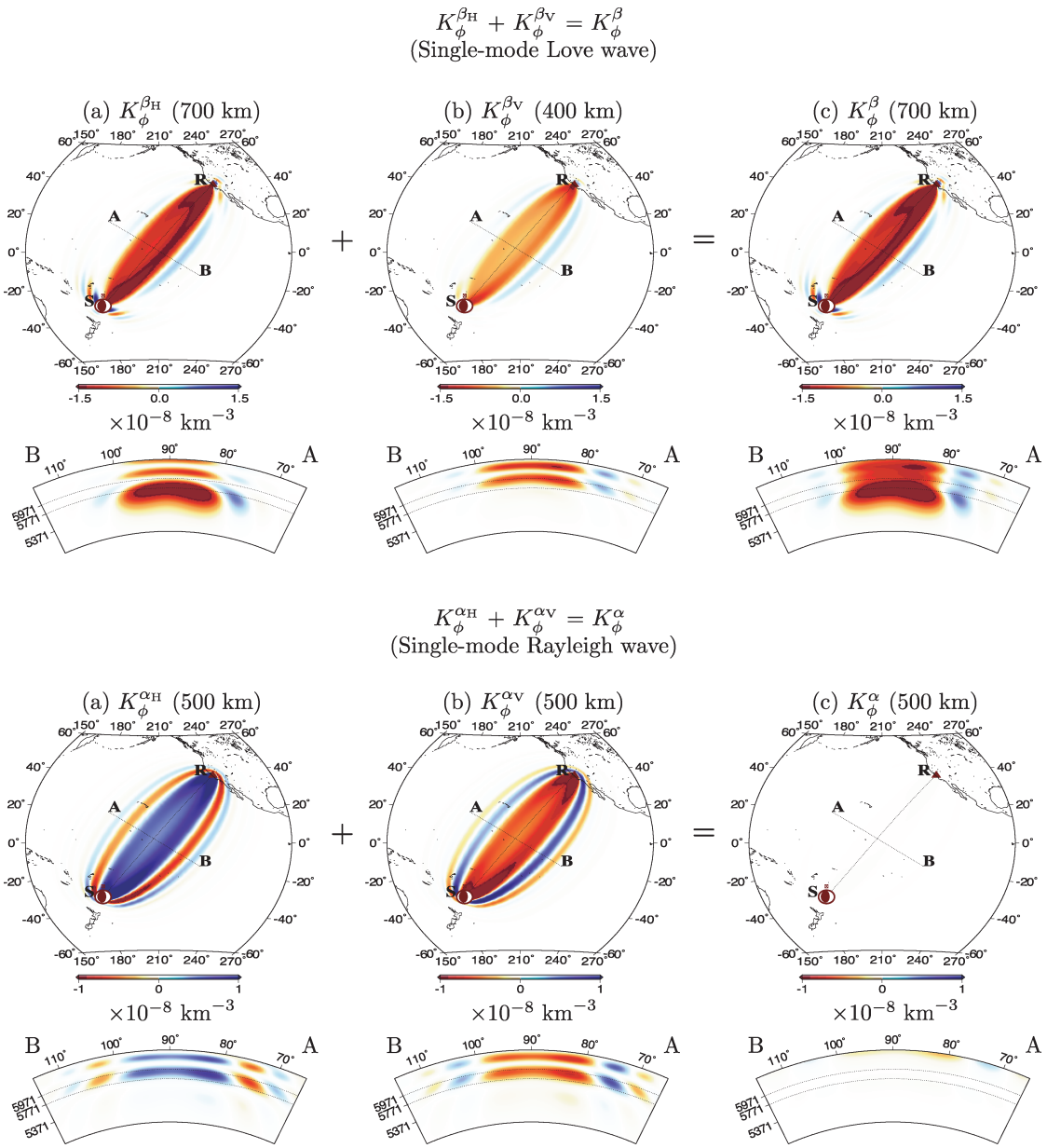

Figure 15. Examples of single-mode Love-wave (top panels) and Rayleigh-wave (bottom panels) sensitivity kernels to anisotropic as well as isotropic velocity perturbations. The sensitivity kernels are computed for 10-mHz phase delays measured with three $3 - \pi$ Slepian multitapers of 500 s, centred at the group arrival of the second higher-mode ($N = 2$) Love (Rayleigh) waves. The source and receiver configurations are the same as in Fig. 1, and the reference earth mode is 1066A (Gilbert & Dziewonski 1975). The sensitivity of Love waves to isotropic *S*-wave velocity perturbations is the sum of the sensitivity to *SH*- and *SV*- velocity perturbations, that is, $K_\phi^\beta = K_\phi^{\beta_H} + K_\phi^{\beta_V}$. The sensitivity kernels $K_\phi^{\beta_H}$ and $K_\phi^{\beta_V}$ are complementary and add up to a stronger isotropic *S*-wave kernel K_ϕ^β. The sensitivity of Rayleigh waves to isotropic *P*-wave velocity perturbations is the sum of the sensitivity to *PH*- and *PV*- velocity perturbations, that is, $K_\phi^\alpha = K_\phi^{\alpha_H} + K_\phi^{\alpha_V}$. The sensitivity of Rayleigh waves to isotropic *P*-wave velocity perturbations is very weak and only confined at shallow depths, due to the opposite polarity of $K_\phi^{\alpha_H}$ and $K_\phi^{\alpha_V}$.

10 DISCUSSION AND CONCLUSION

I develop 3-D Born theory for multimode surface wave observables in radially anisotropic earth model. The sensitivity kernels $K_{\phi,A}^{\beta_H}$, $K_{\phi,A}^{\beta_V}$, $K_{\phi,A}^{\alpha_H}$, $K_{\phi,A}^{\alpha_V}$, $K_{\phi,A}^{\eta}$ and $K_{\phi,A}^{\rho}$—expressing the sensitivity of phase-delay and amplitude measurements to perturbations in wave speeds $\beta_H, \beta_V, \alpha_H, \alpha_V, \eta$ and density ρ—are developed in the framework of surface wave mode summation for multitaper measurements, though the results also apply to single-taper and no-taper (single-frequency) measurements as a special case.

Calculations of both single-mode and multimode surface wave kernels show that waves of different polarizations are coupled in radially anisotropic media. Love waves are most sensitive to *SH* wave speed (β_H); and, their sensitivities to *SV* wave speed (β_V) are significant, especially at shallow depths. Rayleigh waves are most sensitive to *SV* wave speed (β_V), and, their sensitivities to *PH*- and *PV*- wave speeds (α_H and α_V) as well as η are significant.

I show that velocity sensitivity kernels in an isotropic earth model are simply the sum of the sensitivity kernels to anisotropic wave speed perturbations, that is, $K_{\phi,A}^{\alpha} = K_{\phi,A}^{\alpha_H} + K_{\phi,A}^{\alpha_V}$ and

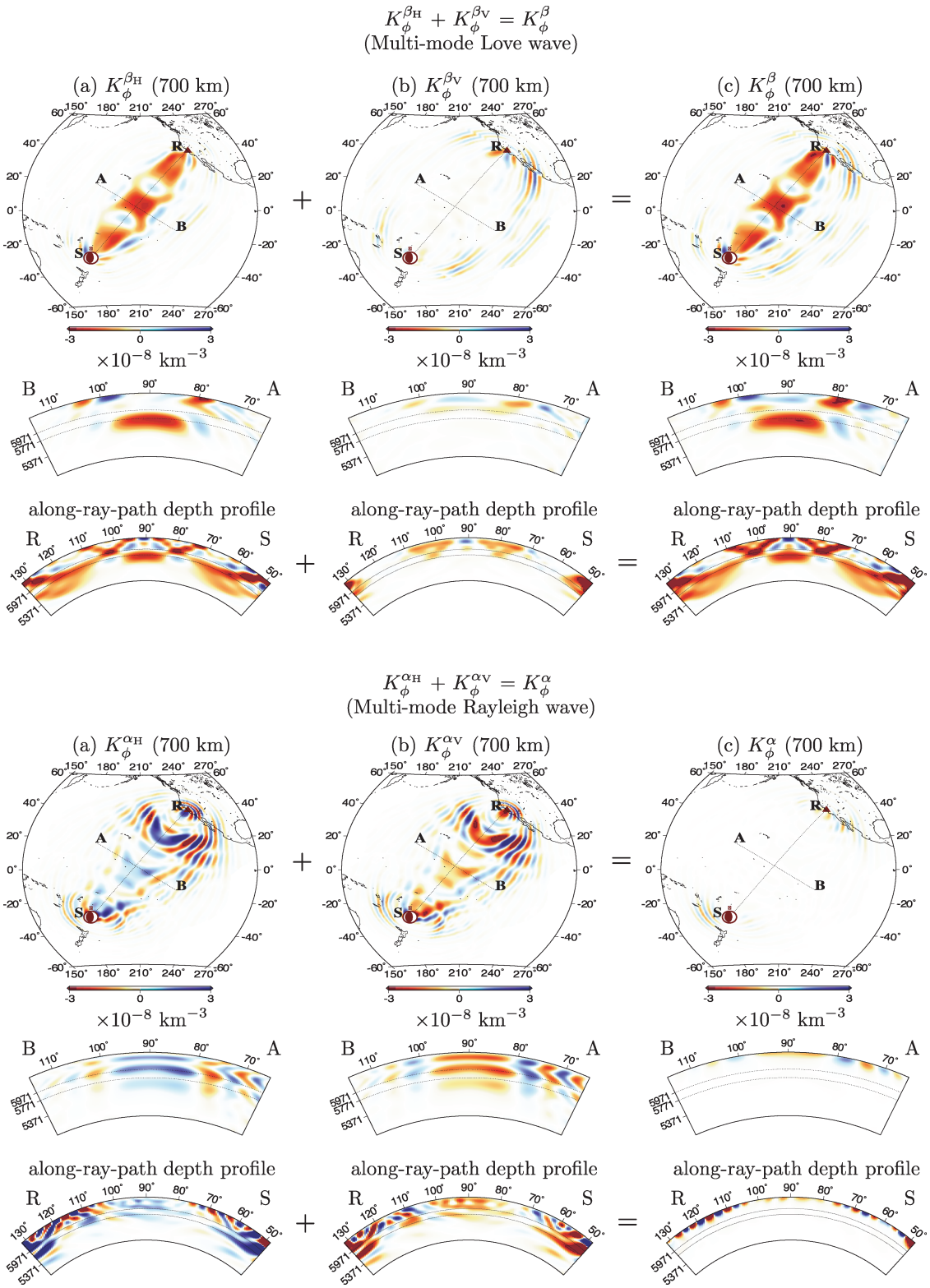

Figure 16. The same as Fig. 15 but for multimode measurements.

$K^{\beta}_{\phi,A} = K^{\beta_H}_{\phi,A} + K^{\beta_V}_{\phi,A}$. The sensitivity kernels of Love waves to *SH*- and *SV*-velocity perturbations are complementary, as a result, Love waves are more sensitive to perturbations in isotropic *S*-wave speed (β) than anisotropic wave speeds (β_H or β_V). The sensitivity kernels of Rayleigh waves to *PH*- and *PV*-velocity perturbations, $K^{\alpha_H}_{\phi,A}$ and $K^{\alpha_V}_{\phi,A}$, have opposite polarities, therefore, Rayleigh-wave sensitivity to isotropic *P*-wave velocity perturbation ($K^{\alpha}_{\phi,A}$) is very small and is confined in regions close to the surface of the Earth.

Calculations of sensitivity kernels of multimode measurements show body wave 'ray' features due to coupling among overtone

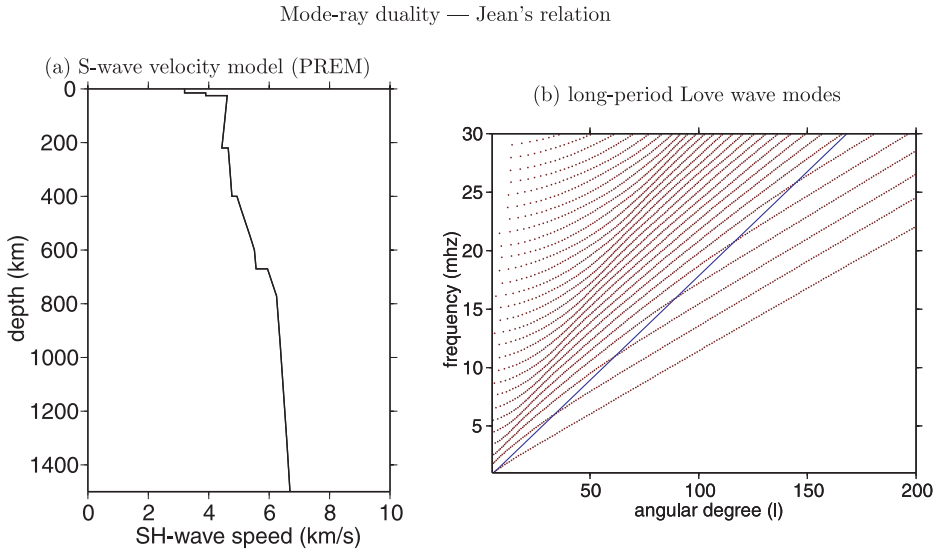

Figure 17. (a) *SH*-wave velocity in the uppermost 1500 km of the reference model (PREM); (b) Long-period Love-wave dispersion diagram computed for the reference model, PREM. The blue line represents a suite of modes that satisfies a frequency–angular degree relation, $\omega = (1/p)\,(l + 1/2)$, with p being the ray parameter computed for rays turning at ∼700 km depth in the reference model. At 10 mHz, the blue line intercepts with the second higher-mode ($N = 2$) Love-wave dispersion curve at an angular degree of $l \approx 55$. Sensitivity kernels of phase delays made with measurement windows centred at the group arrival of the second higher-mode Love wave at different epicentral distances are plotted in Fig. 18.

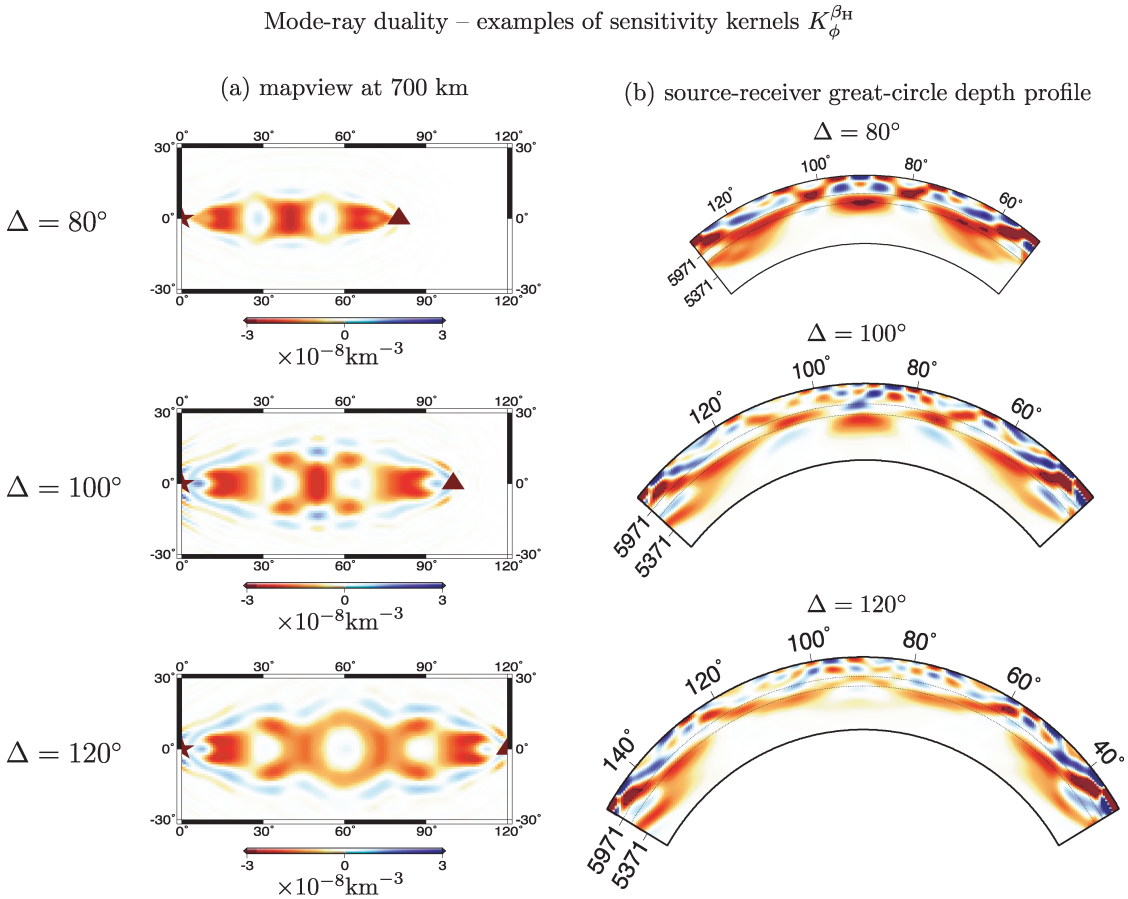

Figure 18. Examples of sensitivity kernels $K_\phi^{\beta_H}$ of measurements made with a 500-s time window centred at the group arrival of the second higher-mode ($N = 2$) Love waves at epicentral distances $\Delta = 80°$, 100° and 120°. Sensitivity kernels are computed for 10-mHz, multimode, Love-wave, phase delays measured with three $3 - \pi$ Slepian multitaper. The along-ray-path profiles show that the second higher-mode Love-wave arrivals at different epicentral distances correspond to different groups of 'rays'. Regardless of epicentral distances, all kernels display a maximum sensitivity at around 700 km depth—the turning depth of the corresponding 'rays' associated with the second overtone mode. The source–receiver configurations are similar to Fig. 1, and all mapviews are plotted in the ray coordinates.

modes, and, phase-delay and amplitude measurements show complementary sensitivity. The connection between 'modes' and 'rays' can be quantified using Jean's relation—which relates the angular order of a 'mode' to the ray parameter of the corresponding 'ray'. Seismic waves can be analysed either as 'rays' or as 'modes'; and, it is the measurement time window that determines the 'turning point' of the 'rays' and the maximum sensitivity depth of the coupled 'modes'. Jean's relation can be applied to determine measurement time windows that maximize data sensitivity in a desired depth range. In general, short-period ($< \sim 50$ s) waves can be more efficiently analysed in the ray framework as the 'ray' features brought out by mode coupling can be stable over the frequency range; and, the number of modes associated with high-frequency waves is large. Long-period ($> \sim 50$ s) waves can be more readily analysed in the mode framework as the number of surface wave modes involved is limited, and the multimode signals are more dispersive. I point out that measurement process should be carefully taken into account in computing multimode sensitivity kernels.

In the case of single-mode measurements, a forward-scattering approximation is used to reduce the exact 3-D sensitivity kernels to 2-D kernels $K^c_{\phi,A}(\hat{\mathbf{r}}, \omega)$, expressing the phase-delay and amplitude sensitivity to local phase-velocity ($\delta c/c$) perturbations. The 2-D kernels can be further reduced to ray theory for single-frequency measurements as shown by Zhou *et al.* (2004).

Multimode sensitive kernels developed in this paper are computed with full mode coupling, the computational expense increases as M^2, where M is the total number of the surface wave modes within the measurement frequency band. This is computationally expensive, especially for relatively high-frequency (e.g. >10 mHz) measurements. A fast computation scheme has been developed to speed up kernel computations for large data set and will be documented in a separate paper (Zhou, in preparation). The development of low-frequency (<20 mHz), multimode surface wave kernels opens the opportunity for imaging high-resolution 3-D structure of velocity and radial anisotropy in the top $\sim$1500 km of the mantle.

ACKNOWLEDGMENTS

I wish to thank the two reviewers, Anne Sieminski and Mark Panning, for their thoughtful and constructive comments which significantly improved the manuscript. This research was financially supported by the US National Science Foundation under Grant EAR-0809464. All maps were generated using the Generic Mapping Tools (GMT) (Wessel & Smith 1995).

REFERENCES

Anderson, D.L., 1961. Elastic wave propagation in layered anisotropic media, *J. geophys. Res.,* **66,** 2953–2963.

Anderson, D.L. & Dziewonski, A.M., 1982. Upper mantle anisotropy: evidence from free oscillations, *Geophys. J. R. astr. Soc.,* **69,** 383–404.

Aki, K. & Kaminuma, K., 1963. Phase velocity of Love waves in Japan (part 1): Love waves from the Aleutian shock of March 1957, *Bull. Earthq. Res. Inst.,* **41,** 243–259.

Aki, K. & Richards, G.R., 2002. *Quantitative Seismology*, 2nd edn, University Science Books, Herndon, VA.

Baig, A. & Dahlen, F., 2004. Statistics of traveltimes and amplitudes in random media, *Geophys. J. Int.,* **158,** 187–210.

Beghein, C. & Trampert, J., 2003. Probability density functions for radial anisotropy: implications for the upper 1200 km of the mantle, *Earth planet. Sci. Lett.,* **217,** 151–162.

Dahlen, F.A. & Baig, A.M., 2002. Fréchet kernels for body wave amplitudes, *Geophys. J. Int.,* **150,** 440–466.

Dahlen, F.A., Hung, S.-H. & Nolet, G., 2000. Fréchet kernels for finite-frequency travel times—I. Theory, *Geophys. J. Int.,* **141,** 157–174.

Dahlen, F.A. & Tromp, J., 1998. *Theoretical Global Seismology*, Princeton University Press, Princeton, NJ.

Dalkolmo, J. & Friederich, W., 2000. Born scattering of long-period body waves, *Geophys. J. Int.,* **142,** 876–888.

Dziewonski, A.M. & Anderson, D.L., 1981. Preliminary reference earth model, *Phys. Earth planet. Inter.,* **25,** 297–356.

Gilbert, F. & Dziewonski, A.M., 1975. An application of normal mode theory to the retrieval of structural parameters and source mechanisms from seismic spectra, *Phil. Trans. R. Soc. Lond. A,* **278,** 187–269.

Hung, S.-H., Dahlen, F.A. & Nolet, G., 2000. Fréchet kernels for finite-frequency travel times—II. Examples, *Geophys. J. Int.,* **141,** 175–203.

Jeans, J.H., 1927. The propagation of earthquake waves, *Proc. Roy. Soc. Lond., Ser. A,* **102,** 554–574.

Laske, G. & Masters, G., 1996. Constraints on global phase velocity maps from long-period polarization data, *J. geophys. Res.,* **101,** 16 059–16 075.

Lebedev, S. & Nolet, G., 2003. Upper mantle beneath southeast Asia from S velocity tomography, *J. geophys. Res.,* **108,** doi:10.1029/2000JB000073.

Lerner-Lam, A.L. & Jordan, T.H., 1983. Earth structure from fundamental and higher-mode waveform analysis, *Geophys. J. R. astr. Soc.,* **75,** 759–797.

Li, X.D. & Romanowicz, B., 1996. Global mantle shear velocity model developed using nonlinear asymptotic coupling theory, *J. geophys. Res.,* **101,** 245–273.

Liu, Q. & Tromp, J., 2008. Finite-frequency Sensitivity kernels for global seismic wave propagation based upon adjoint methods, *Geophys. J. Int.,* **174,** 265–286.

Love, A.E.H., 1927. *A Treatise on the Mathematical Theory of Elasticity*, Cambridge University Press.

Marquering, H., Nolet, G. & Dahlen, F.A., 1998. Three-dimensional waveform sensitivity kernels, *Geophys. J. Int.,* **132,** 521–534.

Meier, T., Lebedev, S., Nolet, G. & Dahlen, F.A., 1997. Diffraction tomography using multimode surface waves, *J. geophys. Res.,* **102,** 8255–8267.

Montagner, J.-P. & Kennett, B.L.N., 1996. How to reconcile body-wave and normal-mode reference Earth models, *Geophys. J. Int.,* **125,** 229–248.

Montelli, R., Nolet, G., Masters, G., Dahlen, F.A. & Hung, S.-H., 2004. Global P and PP traveltime tomography: rays versus waves, *Geophys. J. Int.,* **158,** 637–654.

Nolet, G., 1990. Partitioned waveform inversion and two-dimensional structure under the network of autonomously recording seismographs, *J. geophys. Res.,* **95,** 8499–8512.

Panning, M. & Nolet, G., 2008. Surface wave tomography for azimuthal anisotropy in a strongly reduced parameter space, *Geophys. J. Int.,* **174,** 629–648.

Panning, M. & Romanowicz, B., 2006. A three-dimensional radially anisotropic model of shear velocity in the whole mantle, *Geophys. J. Int.,* **167,** 361–379.

Romanowicz, B., 1987. Multiplet-multiplet coupling due to lateral heterogeneity: asymptotic effects on the amplitude and frequency of the Earth's normal modes, *Geophys. J. R. astr. Soc.,* **90,** 75–100.

Sieminski, A., Liu, Q., Trampert, J. & Tromp, J., 2007. Finite-frequency sensitivity of surface waves to anistropy based upon adjpint methods, *Geophys. J. Int.,* **168,** 1153–1174.

Simons, F.J., van der Hilst, R.D., Montagner, J.P. & Zielhuis, A., 2002. Multimode Rayleigh wave inversion for heterogeneity and azimuthal anisotropy of the Australian upper mantle, *Geophys. J. Int.,* **151,** 738–754.

Slepian, D., 1978. Prolate spheroidal wave functions, Fourier analysis, and uncertainty. V: The discrete case, *Bell Systems Tech. J.,* **57,** 1371–1430.

Spetzler, J., Trampert, J. & Snieder, R., 2002. The effects of scattering in surface wave tomography, *Geophys. J. Int.,* **149,** 755–767.

Snieder, R. & Nolet, G., 1987. Linearized scattering of surface waves on a spherical Earth, *J. geophys.* **61,** 55–63.

Stutzmann, E. & Montagner, J.P., 1994. Tomography of the transition zone from the inversion of higher-mode surface wave, *Phys. Earth planet. Inter.,* **86,** 99–115.

Thomson, D.J., 1982. Spectrum estimation and harmonic analysis, *IEEE Proc.,* **70,** 1055–1096.

Tromp, J. & Dahlen, F.A., 1992. Variational principles for surface wave propagation on a laterally heterogeneous Earth—II. Frequency-domain JWKB theory, *Geophys. J. Int.,* **109,** 599–619.

Tromp, J., Tape, C. & Liu, Q., 2005. Seismic tomography, adjoint methods, time reversal and banana-doughnut kernels, *Geophys. J. Int.,* **160,** 195–216.

van Heijst, H.J. & Woodhouse, J.H., 1997. Measuring surface wave overtone phase velocities using a mode branch stripping technique, *Geophys. J. Int.,* **131,** 209–230.

van Heijst, H.J. & Woodhouse, J.H., 1999. Global high-resolution phase velocity distribution of overtone and fundamental-mode surface waves determined by mode branch stripping, *Geophys. J. Int.,* **137,** 601–620.

Wang, Z. & Dahlen, F.A., 1995. Validity of surface wave ray theory on a laterally heterogeneous Earth, *Geophys. J. Int.,* **123,** 757–773.

Wessel, P. & Smith, W.H.F., 1995. New version of the Generic Mapping Tools released, *EOS, Trans. Am. geophys. Un.,* **76,** 329.

Woodhouse, J.H. & Girnius, T.P., 1982. Surface waves and free-oscillations in a regionalized earth mode, *Geophys. J. R. astr. Soc.,* **68,** 653–673.

Woodhouse, J.H. & Wong, Y.K., 1986. Amplitudes, phase and path anomalies of mantle waves, *Geophys. J. R. astr. Soc.,* **87,** 753–773.

Yomogida, K. & Aki, K., 1987. Amplitude and phase data inversions for phase velocity anomalies in the Pacific Ocean basin, *Geophys. J. R. astr. Soc.,* **88,** 161–204.

Yoshizawa, K. & Kennett, B.L.N., 2005. Sensitivity kernels for finite-frequency surface waves, *Geophys. J. Int.,* **162,** 910–926.

Zhao, L., Jordan, T.H. & Chapman, C.H., 2000. Three-dimension Fréchet differential kernels for seismic delay times, *Geophys. J. Int.,* **141,** 558–576.

Zhou, Y., Dahlen, F.A. & Nolet, G., 2004. Three-dimensional sensitivity kernels for surface wave observables, *Geophys. J. Int.,* **158,** 142–168.

Zhou, Y., Dahlen, F.A., G. Nolet & Laske, G., 2005. Finite-frequency effects in global surface wave tomography, *Geophys. J. Int.,* **163,** 1087–1111.

Zhou, Y., Nolet, G., Dahlen, F.A. & Laske, G., 2006. Global upper-mantle structure from finite-frequency surface wave tomography, *J. geophys. Res.,* **111,** B04304, doi:10.1029/2005JB003677.

APPENDIX A: THE SOURCE AND RECEIVER TERM

In this appendix, I give detailed expressions of the source radiation term and the receiver term introduced in eqs (5) and (22). Those expressions can also be found in Zhou *et al.* (2004). The source radiation term for mode σ is defined as

$$\mathcal{S} = \mathcal{S}_\sigma(\zeta) = (i\omega)^{-1}(\mathbf{M}:\mathbf{E}_s^*), \tag{A1}$$

where ζ is the source take-off angle measured counterclockwise from the South (Fig. A1), the second order tensor $\mathbf{E}_s$ is the surface wave strain tensor (Dahlen & Tromp 1998, section 11.4) evaluated at the source $\mathbf{x}_s$; the asterisk denotes the complex conjugate, and the quantity $\mathbf{M}$ is the source moment tensor. Upon substituting expressions of $\mathbf{E}_s^*$ and $\mathbf{M}$ in eq. (A1), the source radial term becomes

$$\begin{aligned}\mathcal{S} = &-i\,\omega^{-1}\left[\, M_{rr}\dot{U}_s + (M_{\theta\theta}+M_{\phi\phi})r_s^{-1}\left(U_s - \tfrac{1}{2}kV_s\right)\right]\\ &+\omega^{-1}(-1)^n\left(\dot{V}_s - r_s^{-1}V_s + kr_s^{-1}U_s\right)\left(M_{r\phi}\sin\zeta + M_{r\theta}\cos\zeta\right)\\ &+i\,\omega^{-1}kr_s^{-1}V_s\left[\, M_{\theta\phi}\sin 2\zeta + \tfrac{1}{2}(M_{\theta\theta}-M_{\phi\phi})\cos 2\zeta\,\right]\\ &+\omega^{-1}(-1)^n\left(\dot{W}_s - r_s^{-1}W_s\right)\left(M_{r\theta}\sin\zeta - M_{r\phi}\cos\zeta\right)\\ &+i\,\omega^{-1}kr_s^{-1}W_s\left[\tfrac{1}{2}\left(M_{\theta\theta}-M_{\phi\phi}\right)\sin 2\zeta - M_{\theta\phi}\cos 2\zeta\,\right]. \end{aligned}\tag{A2}$$

The displacement eigenfunctions U_s, V_s, W_s of mode σ and their derivatives $\dot{U}_s$, $\dot{V}_s$ and $\dot{W}_s$ are evaluated at the radius of the seismic source, $r = r_s$. The quantities M_{rr}, $M_{\phi\phi}$, $M_{\theta\theta}$, $M_{r\theta}$, $M_{r\phi}$ and $M_{\theta\phi}$ are the six independent elements of the moment tensor $\mathbf{M}(\omega)$.

The receiver polarization term $\mathcal{R}$ is defined as

$$\mathcal{R} = \mathbf{p}_r\cdot\hat{\boldsymbol{\nu}} = \left[\,\hat{\mathbf{r}}_r U_r - i\hat{\mathbf{k}}_r V_r + i(\hat{\mathbf{r}}_r\times\hat{\mathbf{k}}_r)W_r\,\right]\cdot\hat{\boldsymbol{\nu}}, \tag{A3}$$

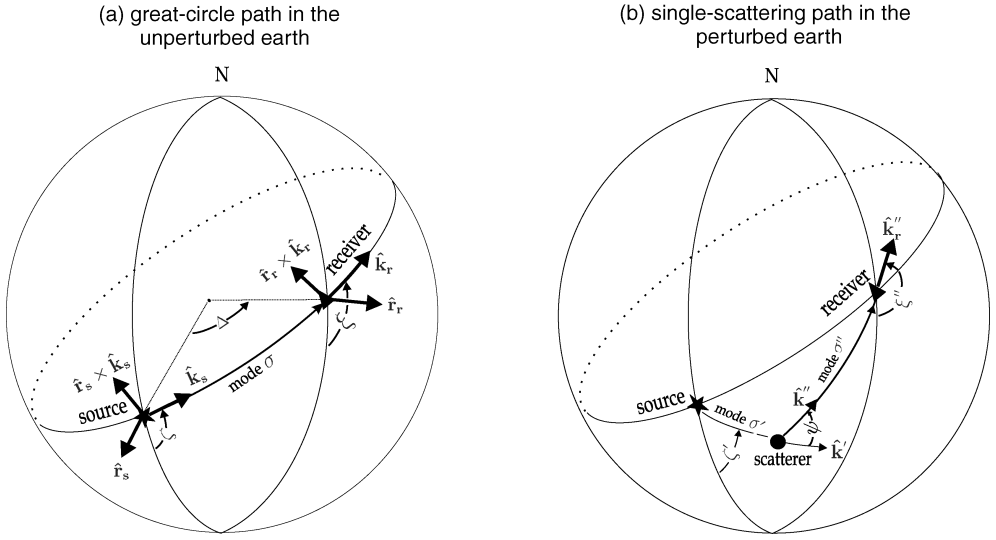

Figure A1. (a) Source–receiver great-circle path in the unperturbed earth. The vectors $\hat{\mathbf{r}}$, $\hat{\mathbf{k}}$ and $\hat{\mathbf{r}}\times\hat{\mathbf{k}}$ are the vertical, radial and transverse unit vectors; roman subscripts s and r denote evaluation at the source or the receiver; σ is the surface wave mode index of the reference ray; Δ is the source–receiver epicentral distance; ζ is the source takeoff angle of the reference ray, measured counterclockwise from geographical south to $\hat{\mathbf{k}}_s$; and ξ is the receiver arrival angle of the reference ray, measured counterclockwise from geographical south to $\hat{\mathbf{k}}_r$. (b) Single-scattering path in the perturbed earth; σ' is the mode index of the outgoing wave along the source-to-scatterer path, σ'' is the mode index of the scattered wave along the scatterer-to-receiver path; $\hat{\mathbf{k}}'$ and $\hat{\mathbf{k}}''$ are the unit wavenumber vectors of modes σ' and σ'', evaluated at the scatterer; $\hat{\mathbf{k}}_r''$ is the unit wavenumber vector of the scattered surface wave mode σ'' at the receiver; ζ' is the source takeoff angle of the outgoing surface wave mode σ'; ξ'' is the receiver arrival angle of the scattered surface wave mode σ''; ψ is the scattering angle, measured counterclockwise from $\hat{\mathbf{k}}'$ to $\hat{\mathbf{k}}''$.

where U_r, V_r and W_r are the displacement eigenfunction of surface wave mode σ evaluated at the radius of the receiver, $r = r_r$. For the reference wave in the spherically symmetric background earth model, the seismometer polarization of vertical, radial and transverse component seismic recordings are

$$\hat{\boldsymbol{\nu}} = \begin{cases} \hat{\mathbf{r}}_r & \text{vertical component,} \\ \hat{\mathbf{k}}_r & \text{radial component,} \\ \hat{\mathbf{r}}_r \times \hat{\mathbf{k}}_r & \text{transverse component;} \end{cases} \tag{A4}$$

and the associated receiver term $\mathcal{R} = \mathcal{R}_\sigma$ for the reference wave in the spherical background model is is given by

$$\mathcal{R} = \begin{cases} U_r & \text{vertical component,} \\ -i\,V_r & \text{radial component,} \\ i\,W_r & \text{transverse component.} \end{cases} \tag{A5}$$

and the associated receiver term for the scattered wave becomes

$$\mathcal{R}'' = \begin{cases} U''_r & \text{vertical component,} \\ -i\,V''_r\cos(\xi''-\xi) - i\,W''_r\sin(\xi''-\xi) & \text{radial component,} \\ i\,W''_r\cos(\xi''-\xi) - i\,V''_r\sin(\xi''-\xi) & \text{transverse component,} \end{cases} \tag{A6}$$

where $U''_r = U_{\sigma''}(r_r)$, $V''_r = V_{\sigma''}(r_r)$, $W''_r = W_{\sigma''}(r_r)$, and ξ'' and ξ are the receiver arrival angles of the scattered wave (σ''th mode) and the reference wave (σth mode), respectively, both measured counterclockwise from geographical south (Fig. A1).

APPENDIX B: THE INTERACTION TERM ${}_{\sigma'}\boldsymbol{\Omega}_{\sigma''}$

The interaction term given in eq. (16) is rewritten below:

$${}_{\sigma'}\Omega_{\sigma''} = \delta\rho\,\omega^2\,(\mathbf{p}'\cdot\,\mathbf{p}''^*) - \mathbf{E}''^*:\delta\mathbf{C}:\mathbf{E}' \tag{B1}$$

where the asterisk denotes the complex conjugate; and and $'$ and $''$ indicate surface wave mode σ' in the source-to-scatterer and mode σ'' in the scatterer-to-receiver leg, respectively; the quantity $\mathbf{p}' = \hat{\mathbf{r}}U' - i\,\hat{\mathbf{k}}'V' + i\,(\hat{\mathbf{r}}\times\hat{\mathbf{k}}')W'$ is the polarization vector of surface wave mode σ' in the source-to-scatterer leg; and $\mathbf{p}'' = \hat{\mathbf{r}}U'' - i\,\hat{\mathbf{k}}''V'' + i\,(\hat{\mathbf{r}}\times\hat{\mathbf{k}}'')W''$ is the polarization vector of surface wave mode σ'' in the scatterer-to-receiver leg. The quantity $\mathbf{E}$ is the surface wave strain tensor as defined in Dahlen & Tromp (1998, section 11.4); the quantity $\delta\mathbf{C}$ is the perturbation in elastic tensor in radially anisotropic media,

$$\begin{aligned}\delta\mathbf{C} = {}& \delta C\hat{\mathbf{r}}\hat{\mathbf{r}}\hat{\mathbf{r}}\hat{\mathbf{r}} + \delta A(\hat{\theta}\hat{\theta}\hat{\theta}\hat{\theta} + \hat{\phi}\hat{\phi}\hat{\phi}\hat{\phi}) \\ & + \delta F(\hat{\mathbf{r}}\hat{\mathbf{r}}\hat{\theta}\hat{\theta} + \hat{\theta}\hat{\theta}\hat{\mathbf{r}}\hat{\mathbf{r}} + \hat{\mathbf{r}}\hat{\mathbf{r}}\hat{\phi}\hat{\phi} + \hat{\phi}\hat{\phi}\hat{\mathbf{r}}\hat{\mathbf{r}}) \\ & + (\delta A - 2\delta N)(\hat{\theta}\hat{\theta}\hat{\phi}\hat{\phi} + \hat{\phi}\hat{\phi}\hat{\theta}\hat{\theta}) \\ & + \delta N(\hat{\theta}\hat{\phi}\hat{\theta}\hat{\phi} + \hat{\phi}\hat{\theta}\hat{\phi}\hat{\theta} + \hat{\theta}\hat{\phi}\hat{\phi}\hat{\theta} + \hat{\phi}\hat{\theta}\hat{\theta}\hat{\phi}) \\ & + \delta L(\hat{\mathbf{r}}\hat{\theta}\hat{\mathbf{r}}\hat{\theta} + \hat{\theta}\hat{\mathbf{r}}\hat{\theta}\hat{\mathbf{r}} + \hat{\mathbf{r}}\hat{\theta}\hat{\theta}\hat{\mathbf{r}} + \hat{\theta}\hat{\mathbf{r}}\hat{\mathbf{r}}\hat{\theta} \\ & \quad + \hat{\mathbf{r}}\hat{\phi}\hat{\mathbf{r}}\hat{\phi} + \hat{\phi}\hat{\mathbf{r}}\hat{\phi}\hat{\mathbf{r}} + \hat{\mathbf{r}}\hat{\phi}\hat{\phi}\hat{\mathbf{r}} + \hat{\phi}\hat{\mathbf{r}}\hat{\mathbf{r}}\hat{\phi}),\end{aligned} \tag{B2}$$

and all quantities in eq. (B1) are evaluated at the scatterer.

To the first order, perturbations in the elastic constants A, C, N, L and F can be related to perturbations in anisotropic wave speed using eq. (6).

$$\begin{aligned}&\delta A = \delta\rho\alpha_H^2 + 2\rho\alpha_H\delta\alpha_H, \quad \delta C = \delta\rho\alpha_V^2 + 2\rho\alpha_V\delta\alpha_V, \\ &\delta N = \delta\rho\beta_H^2 + 2\rho\beta_H\delta\beta_H, \quad \delta L = \delta\rho\beta_V^2 + 2\rho\beta_V\delta\beta_V, \\ &\delta F = \delta\eta(A-2L) + \eta(\delta A - 2\delta L).\end{aligned} \tag{B3}$$

Upon substituting eqs (B3) and (B2) in eq. (B1), the interaction term ${}_{\sigma'}\Omega_{\sigma''}$ can be expressed as a linear combination of fractional perturbations $\delta\alpha_H/\alpha_H, \delta\alpha_V/\alpha_V, \delta\beta_H/\beta_H, \delta\beta_V/\beta_V, \delta\eta/\eta$ and $\delta\rho/\rho$:

$$\begin{aligned}{}_{\sigma'}\Omega_{\sigma''} = {}& {}_{\sigma'}\Omega^m_{\sigma''}\delta m = {}_{\sigma'}\Omega^{\alpha_H}_{\sigma''}\left(\frac{\delta\alpha_H}{\alpha_H}\right) + {}_{\sigma'}\Omega^{\alpha_V}_{\sigma''}\left(\frac{\delta\alpha_V}{\alpha_V}\right) \\ & + {}_{\sigma'}\Omega^{\beta_H}_{\sigma''}\left(\frac{\delta\beta_H}{\beta_H}\right) + {}_{\sigma'}\Omega^{\beta_V}_{\sigma''}\left(\frac{\delta\beta_V}{\beta_V}\right) + {}_{\sigma'}\Omega^{\eta}_{\sigma''}\left(\frac{\delta\eta}{\eta}\right) \\ & + {}_{\sigma'}\Omega^{\rho}_{\sigma''}\left(\frac{\delta\rho}{\rho}\right),\end{aligned} \tag{B4}$$

where ${}_{\sigma'}\Omega^{\alpha_V}_{\sigma''}$, ${}_{\sigma'}\Omega^{\alpha_H}_{\sigma''}$, ${}_{\sigma'}\Omega^{\beta_V}_{\sigma''}$, ${}_{\sigma'}\Omega^{\beta_H}_{\sigma''}$, ${}_{\sigma'}\Omega^{\eta}_{\sigma''}$ and ${}_{\sigma'}\Omega^{\rho}_{\sigma''}$ are the scattering coefficients. For Love-to-Love scattering,

$${}_{\sigma'}\Omega^{\alpha_H}_{\sigma''} = 0;$$

$${}_{\sigma'}\Omega^{\alpha_V}_{\sigma''} = 0;$$

$${}_{\sigma'}\Omega^{\beta_H}_{\sigma''} = -2\rho\beta_H^2\;k'k''r^{-2}W'W''\cos 2\psi;$$

$${}_{\sigma'}\Omega^{\beta_V}_{\sigma''} = -2\rho\beta_V^2\,(\dot{W}' - r^{-1}W')(\dot{W}'' - r^{-1}W'')\cos\psi$$

$${}_{\sigma'}\Omega^{\eta}_{\sigma''} = 0$$

$$\begin{aligned}{}_{\sigma'}\Omega^{\rho}_{\sigma''} = {}& \rho\omega^2 W'W''\cos\psi \\ & - \rho\beta_V^2(\dot{W}' - r^{-1}W')(\dot{W}'' - r^{-1}W'')\cos\psi \\ & - \rho\beta_H^2 k'k''r^{-2}W'W''\cos 2\psi;\end{aligned}$$

for Rayleigh-to-Rayleigh scattering,

$$\begin{aligned}{}_{\sigma'}\Omega^{\alpha_H}_{\sigma''} = {}& -2\rho\alpha_H^2 r^{-2}(2U' - k'V')(2U'' - k''V'') \\ & - 2\rho\alpha_H^2\eta r^{-1}[\,\dot{U}'(2U'' - k''V'') + \dot{U}''(2U' - k'V')\,]\end{aligned}$$

$${}_{\sigma'}\Omega^{\alpha_V}_{\sigma''} = -2\rho\alpha_V^2\dot{U}'\dot{U}''$$

$$\begin{aligned}{}_{\sigma'}\Omega^{\beta_H}_{\sigma''} = {}& 2\rho\beta_H^2 r^{-2}(2U' - k'V')(2U'' - k''V'') \\ & - 2\rho\beta_H^2 r^{-2}k'k''V'V''\cos 2\psi\end{aligned}$$

$$\begin{aligned}{}_{\sigma'}\Omega^{\beta_V}_{\sigma''} = {}& 4\rho\beta_V^2\eta r^{-1}[\,\dot{U}'(2U'' - k''V'') + \dot{U}''(2U' - k'V')\,] \\ & - 2\rho\beta_V^2(\dot{V}' - r^{-1}V' + r^{-1}k'U')(\dot{V}'' - r^{-1}V'' \\ & \quad + r^{-1}k''U'')\cos\psi\end{aligned}$$

$${}_{\sigma'}\Omega^{\eta}_{\sigma''} = \left(2\rho\beta_V^2 - \rho\alpha_H^2\right)\eta r^{-1}[\,(\dot{U}'(2U'' - k''V'') + \dot{U}''(2U' - k'V')]$$

$$\begin{aligned}{}_{\sigma'}\Omega^{\rho}_{\sigma''} = {}& \rho\omega^2(U'U'' + V'V''\cos\psi) - \rho\alpha_V^2\dot{U}'\dot{U}'' \\ & - \rho(\alpha_H^2 + \beta_H^2)r^{-2}[(2U' - k'V')(2U'' - k''V'')] \\ & - rho(\alpha_H^2 - \beta_V^2)\eta r^{-1}[\dot{U}'(2U' - k'V') + \dot{U}''(2U'' - k''V'')] \\ & - \rho\beta_V^2(\dot{V}' - r^{-1}V' + k'r^{-1}U')(\dot{V}'' - r^{-1}V'' \\ & \quad + k''r^{-1}U'')\cos\psi \\ & - \rho\beta_H^2 k'k''r^{-2}V'V''\cos 2\psi;\end{aligned}$$

for Love-to-Rayleigh scattering,

$$_{\sigma'}\Omega^{\alpha_{\rm H}}_{\sigma''} = 0;$$

$$_{\sigma'}\Omega^{\alpha_{\rm V}}_{\sigma''} = 0;$$

$$_{\sigma'}\Omega^{\beta_{\rm H}}_{\sigma''} = 2\rho\beta_{\rm H}^2 r^{-2} k' k'' W' V'' \sin 2\psi;$$

$$_{\sigma'}\Omega^{\beta_{\rm V}}_{\sigma''} = 2\rho\beta_{\rm V}^2 (\dot{W}' - r^{-1}W')(\dot{V}'' - r^{-1}V'' + k'' r^{-1}U'') \sin\psi;$$

$$_{\sigma'}\Omega^{\eta}_{\sigma''} = 0;$$

$$\begin{aligned} _{\sigma'}\Omega^{\rho}_{\sigma''} = & -\rho\omega^2 W' V'' \sin\psi \\ & + \rho\beta_{\rm V}^2 (\dot{W}' - r^{-1}W')(\dot{V}'' - r^{-1}V'' + k'' r^{-1}U'') \sin\psi \\ & + \rho\beta_{\rm H}^2 k' k'' r^{-2} W' V'' \sin 2\psi; \end{aligned}$$

for Rayleigh-to-Love scattering,

$$_{\sigma'}\Omega^{\alpha_{\rm H}}_{\sigma''} = 0;$$

$$_{\sigma'}\Omega^{\alpha_{\rm V}}_{\sigma''} = 0;$$

$$_{\sigma'}\Omega^{\beta_{\rm H}}_{\sigma''} = -2\rho\beta_{\rm H}^2 r^{-2} k' k'' V' W'' \sin 2\psi;$$

$$_{\sigma'}\Omega^{\beta_{\rm V}}_{\sigma''} = -2\rho\beta_{\rm V}^2 (\dot{V}' - r^{-1}V' + k' r^{-1}U')(\dot{W}'' - r^{-1}W'') \sin\psi;$$

$$_{\sigma'}\Omega^{\eta}_{\sigma''} = 0;$$

$$\begin{aligned} _{\sigma'}\Omega^{\rho}_{\sigma''} = & \rho\omega^2 V' W'' \sin\psi \\ & - \rho\beta_{\rm V}^2 (\dot{V}' - r^{-1}V' + k' r^{-1}U')(\dot{W}'' - r^{-1}W'') \sin\psi \\ & - \rho\beta_{\rm H}^2 k' k'' r^{-2} V' W'' \sin 2\psi. \end{aligned}$$

The quantity $\psi = \arccos(\hat{\mathbf{k}}' \cdot \hat{\mathbf{k}}'')$ is the scattering angle, measured counterclockwise from $\hat{\mathbf{k}}'$ to $\hat{\mathbf{k}}''$ (Fig. A1).